

Constraining the mass of the M31 ionized baryon Halo using CHIME/FRB Catalog 2

LORDRICK A. KAHINGA ^{1,2}, J. XAVIER PROCHASKA ^{1,3,4}, SUNIL SIMHA ^{5,6,*}, CALVIN LEUNG ^{7,†}, RADU V. CRAIU ⁸,
GWENDOLYN. EADIE ^{9,8}, EMMANUEL FONSECA ^{10,11}, B. M. GAENSLER ^{1,9,12}, VICKY KASPI ^{13,14}, AFROKK KHAN ^{13,14},
BIKASH KHAREL ^{10,11}, ADAM E. LANMAN ^{15,16}, ROBERT A. MAIN ^{13,14}, LLUIS MAS-RIBAS ¹, KIYOSHI W. MASUI ^{15,16},
PAUL SCHOLZ ¹⁷, SWARALI SHIVRAJ PATIL ^{10,11}, AARON B. PEARLMAN ^{15,16,13,14,‡}, K. SHIN ¹⁸, SETH R. SIEGEL ^{19,13,14},
KENDRICK SMITH ¹⁹ AND MICHELE WOODLAND ¹

¹Department of Astronomy and Astrophysics, University of California, Santa Cruz, 1156 High Street, Santa Cruz, CA 95064, USA

²Department of Physics, College of Natural and Mathematical Sciences, University of Dodoma, Dodoma, P.O. Box 259, Tanzania

³Kavli Institute for the Physics and Mathematics of the Universe (Kavli IPMU), 5-1-5 Kashiwanoha, Kashiwa, 277-8583, Japan

⁴Division of Science, National Astronomical Observatory of Japan, 2-21-1 Osawa, Mitaka, Tokyo 181-8588, Japan

⁵Center for Interdisciplinary Exploration and Research in Astronomy, Northwestern University, 1800 Sherman Avenue, Evanston, IL 60201, USA

⁶Department of Astronomy and Astrophysics, University of Chicago, William Eckhart Research Center, 5640 South Ellis Avenue, Chicago, IL 60637, USA

⁷Department of Astronomy, University of California, Berkeley, CA 94720, United States

⁸Department of Statistical Sciences, University of Toronto, 700 University Ave., Toronto, ON M5G 1Z5, Canada

⁹David A. Dunlap Department of Astronomy and Astrophysics, 50 St. George Street, University of Toronto, ON M5S 3H4, Canada

¹⁰Department of Physics and Astronomy, West Virginia University, PO Box 6315, Morgantown, WV 26506, USA

¹¹Center for Gravitational Waves and Cosmology, West Virginia University, Chestnut Ridge Research Building, Morgantown, WV 26505, USA

¹²Dunlap Institute for Astronomy and Astrophysics, 50 St. George Street, University of Toronto, ON M5S 3H4, Canada

¹³Department of Physics, McGill University, 3600 rue University, Montréal, QC H3A 2T8, Canada

¹⁴Trottier Space Institute, McGill University, 3550 rue University, Montréal, QC H3A 2A7, Canada

¹⁵MIT Kavli Institute for Astrophysics and Space Research, Massachusetts Institute of Technology, 77 Massachusetts Ave, Cambridge, MA 02139, USA

¹⁶Department of Physics, Massachusetts Institute of Technology, 77 Massachusetts Ave, Cambridge, MA 02139, USA

¹⁷Department of Physics and Astronomy, York University, 4700 Keele Street, Toronto, ON M3J 1P3, Canada

¹⁸Cahill Center for Astronomy and Astrophysics, MC 249-17 California Institute of Technology, Pasadena CA 91125, USA

¹⁹Perimeter Institute of Theoretical Physics, 31 Caroline Street North, Waterloo, ON N2L 2Y5, Canada

ABSTRACT

The circumgalactic medium (CGM) surrounding galaxies is believed to be a significant reservoir of baryons, yet its total mass remains poorly constrained. We present a novel approach to probe the CGM of the Andromeda galaxy (M31) using fast radio bursts (FRBs) from the CHIME/FRB Catalog 2. By comparing the dispersion measures (DMs) of 171 FRBs whose sightlines intersect M31’s halo (within $r_{\text{vir}} = 302$ kpc) to a control sample of 684 FRBs, we estimate the DM contribution from M31’s CGM. We find evidence for an excess DM of $\delta\text{DM} = 5.9\text{--}59.6$ pc cm⁻³ in the inner halo ($\approx 0\text{--}151$ kpc) and $\delta\text{DM} = 25.7\text{--}64.6$ pc cm⁻³ in the outer halo ($\approx 151\text{--}302$ kpc). Using a generalized halo model parameterized by a closure radius r_{close} , we constrain the baryon distribution and infer a best-fit value for r_{close} to be $9.2^{+9.9}_{-4.9} r_{\text{vir}}$ (1σ), corresponding to a total CGM mass of $M_{b,\text{halo}} = 18.6^{+7.9}_{-8.4} \times 10^{10} M_{\odot}$. Our results suggest that M31 may harbor a substantial fraction of its cosmic baryon budget in diffuse, ionized gas. This work demonstrates the potential of FRBs as a powerful tool for studying the CGM of nearby galaxies, with future larger samples expected to provide tighter constraints on the baryon content of galactic halos.

Keywords: Circumgalactic medium – Fast radio bursts – Andromeda Galaxy – Galaxy halos – Dispersion measure

Corresponding author: Lordrick A. Kahinga

lkahinga@ucsc.edu

* NU-UC Brinson Fellow

† NHFP Einstein Fellow

‡ NASA Hubble Fellow.

1. INTRODUCTION

The circumgalactic medium (CGM) is a diffuse, multiphase gas that surrounds galaxies and extends out to their virial radii and beyond (e.g., [Wilde et al. 2021](#)). It carries information regarding the history of a galaxy, both as a reservoir for gas that fuels star formation and as a repository for material ejected by feedback processes (see reviews by [Tumlinson et al. 2017](#); [Péroux & Howk 2020](#); [Chen & Zahedy 2024](#); [Faucher-Giguère & Oh 2023](#)). The CGM serves as a bridge between galaxies and the more diffuse intergalactic medium, and is therefore a crucial region for the exchange of baryons and metals due to galactic feedback and interactions, playing a significant role in the evolution of galaxies (e.g., [Prochaska et al. 2011](#); [Lehner et al. 2015](#); [Tchernyshyov et al. 2023](#); [Zhang et al. 2024a](#); [Medlock et al. 2024](#)).

Another key motivation for studying the CGM is that it may be the dominant baryonic component of galactic halos. Observations of the Cosmic Microwave Background (CMB) (e.g., [Komatsu et al. 2011](#); [Planck Collaboration et al. 2020](#)) constrain the universal ratio of baryonic to total matter density, $\Omega_b/\Omega_m \approx 0.158$ ([Planck Collaboration et al. 2020](#)). If galaxies retain their cosmological share of baryons, we expect a halo of total mass M_{halo} to contain a baryonic mass of $M_{b,\text{cosmic}} \equiv M_{\text{halo}}(\Omega_b/\Omega_m)$, which we refer to as the cosmic baryonic mass (following [Chiu et al. 2018](#)). For Milky Way-mass galaxies (commonly referred to as L^* galaxies, with stellar masses $\sim 10^{10.5} M_\odot$ and halo masses $\sim 10^{12} M_\odot$), the mass in galaxies comprising stars, dust, and the interstellar medium (ISM) accounts for only a small fraction of $M_{b,\text{cosmic}}$, since the total halo mass is dominated by dark matter with baryons comprising at most $\sim 16\%$. Yet observations indicate that the stellar and ISM components together typically represent only $\sim 20\text{--}30\%$ of the expected baryonic mass within the virial radius. This so-called galactic missing baryons problem ([McGaugh et al. 2010](#); [Behroozi et al. 2019](#)) implies that either the majority of baryons are in the CGM or the processes of galaxy formation have driven the gas from the system altogether (e.g., [Khrykin et al. 2024a](#)). Therefore, assessing the mass of the CGM in galactic halos lies central to fundamental issues in galaxy formation.

Despite its well-recognized importance, measuring the mass of the CGM has proven very challenging. Part of the difficulty is due to its multiphase nature, i.e., it contains gas at a range of temperatures, densities and ionization states, namely: cool gas ($T < 10^5$ K), warm-hot gas (10^5 K $< T < 10^6$ K), and hot phase $T > 10^6$ K (see review by [Putman et al. 2012](#)). The cool and warm phases are accessible to absorption-line experiments that utilize bright background sources (primarily quasars) to probe the CGM. Measurements by [Tumlinson et al. \(2013\)](#); [Werk et al. \(2013\)](#); [Bordoloi et al. \(2014\)](#); [Liang & Chen \(2014\)](#); [Werk et al. \(2014, 2016\)](#); [Prochaska et al. \(2017\)](#); [Chen et al. \(2020\)](#); [Faerman et al. \(2020\)](#); [Faerman &](#)

[Werk \(2023\)](#); [Qu et al. \(2024\)](#); [Zheng et al. \(2024\)](#) have provided valuable constraints on the warm and cool phases of the CGM. However, these measurements are limited by the brightness of the background sources and the number of sightlines available to probe the CGM of interest. Furthermore, mass estimates require significant ionization corrections and/or assumptions on the gas metallicity ([Werk et al. 2014](#); [Burchett et al. 2016](#)). Nevertheless, current experiments have estimated the cool CGM to contain $\approx 30\%$ of $M_{b,\text{cosmic}}$ in low-redshift, L^* galaxies ([Werk et al. 2014](#)).

Recent studies tracing O VI and Ne VIII absorption have inferred that the warm-hot phase of the CGM (with temperatures $T \sim 10^5\text{--}10^6$ K) may contain an additional $\sim 20\text{--}30\%$ of the baryonic budget ([Faerman et al. 2020](#); [Faerman & Werk 2023](#); [Qu et al. 2024](#)). These estimates are sensitive to assumptions about gas ionization conditions and metallicity. Still, they suggest that the warm phase may be at least as massive as the cool component, and more spatially extended.

Measurements of the hot CGM in L^* galaxies have relied on X-ray observations (e.g., [Anderson & Bregman 2011](#); [Bregman et al. 2018](#)). Most recently, [Zhang et al. \(2024b\)](#) utilized observations from the SRG/eROSITA All-Sky Surveys (eRASS:4) to measure the X-ray surface brightness and detect the hot CGM for L^* galaxies. Their best estimates suggest that the hot CGM is less than $\approx 20\%$ of $M_{b,\text{cosmic}}$, however these measurements depend on assumptions for the metallicity of the CGM, as well as the temperature of the halo.

With measuring the mass of the CGM as our primary motivation, we have designed an experiment that focuses on the Andromeda galaxy (M31), the massive spiral galaxy located at a distance of 752 kpc ([Riess et al. 2012](#)) from Earth. The galaxy’s rotation curve and satellite dynamics suggest a total halo mass in the range $(1.5\text{--}3) \times 10^{12} M_\odot$ ([van der Marel et al. 2012](#); [Patel & Mandel 2023](#)), making it the nearest large galaxy outside the Milky Way. M31 has been extensively studied across multiple wavelengths, yielding insights into its stellar disk, bulge, halo, and dark matter distribution ([Renda et al. 2005](#); [Wada & Combes 2008](#); [Huo et al. 2013](#)). The stellar disk of M31 has been mapped in extraordinary detail by the Panchromatic Hubble Andromeda Treasury (PHAT) survey ([Dalcanton et al. 2012](#)), which resolved over 100 million stars across a significant portion of the galaxy. Subsequent studies in the PHAT series have characterized the spatially resolved structure, stellar populations, and dust content of the galaxy ([Williams et al. 2012](#); [Dalcanton et al. 2015](#); [Lewis et al. 2015](#); [Williams et al. 2017](#)). PHAT XIX ([Williams et al. 2017](#)) used color-magnitude diagram fitting of these resolved stars to derive the star formation history of M31’s disk. They estimate that a total of $(1.5 \pm 0.2) \times 10^{11} M_\odot$ of stars have formed over the galaxy’s history, of which $(9 \pm 2) \times 10^{10} M_\odot$ have likely survived to the present. These properties make M31 a natural

laboratory for testing whether massive galaxies retain their expected fraction of baryons during their evolution.

Furthermore, M31’s proximity and therefore large angular extent in the sky (with a halo subtending over 23° corresponding to its virial radius of 302 kpc) make it the best candidate to resolve its CGM with multiple intersecting sightlines from background sources (Lehner et al. 2015, 2020). Observational studies using absorption-line spectroscopy of background quasars (Lehner et al. 2015; Howk et al. 2017; Lehner et al. 2020, 2025) indicate that M31’s circumgalactic medium (CGM) contains a substantial reservoir of gas. Lehner et al. (2025) have probed the cool CGM using Si II, Si III, and Si IV absorption lines, and the warm CGM using O VI. The detection of O VI beyond one virial radius suggests the presence of highly ionized gas extending well into the outer halo. They estimate the baryonic mass of the cool and warm CGM to be $\geq 3.7 \times 10^{10} (Z/0.3Z_\odot)^{-1} M_\odot$. Assuming a dark-matter halo mass ($M_{\text{halo}} = 1.54 \times 10^{12} M_\odot$) (van der Marel et al. 2012); and a metallicity of $0.3Z_\odot$, the mass estimated for warm and cool phases accounts for $\approx 30\%$ of the baryons in the CGM of M31.

Regarding the hot gas associated with M31, Bregman & Lloyd-Davies (2007) and more recently Qu et al. (2021) combine X-ray emission spectra from highly ionised ions (e.g., O VI and O VII) and Sunyaev-Zel’dovich (SZ) and claim a “baryon bridge” connecting the M31 and MW galaxies. This structure can be approximated by a cylinder with a radius of 120 kpc and a length of 400 kpc. They estimate a temperature of $\log T(\text{K}) = 6.34 \pm 0.03$, a density ranging from 10^{-4} cm^{-3} to 10^{-3} cm^{-3} , a metallicity between $0.02Z_\odot$ and $0.1Z_\odot$, and a baryon mass of at least $10^{11} M_\odot$. However, there are significant uncertainties in the measurements of the SZ signal and the estimated column densities from the X-ray emission spectra of ionised metals.

To advance upon these previous works, we here leverage a large sample of fast radio bursts (FRBs) derived from the CHIME/FRB project (CHIME/FRB Collaboration et al. 2018). FRBs are highly energetic, extragalactic bursts that last only a few milliseconds to microseconds (Lorimer et al. 2007). As they traverse through diffuse and ionized plasma, their light disperses with the delay (Δt) in the FRB pulse a function of the pulse frequency ν given by $\Delta t = 4.148808 \text{ ms} \left(\frac{\Delta\nu}{\text{GHz}} \right)^{-2} \left(\frac{\text{DM}}{\text{pc cm}^{-3}} \right)$. The proportionality constant DM is the dispersion measure, which is the sightline integration of the electron density weighted by the cosmological scale factor

$$\text{DM} = \int \frac{n_e}{1+z} ds \quad (1)$$

(e.g., Petroff et al. 2014; Chatterjee et al. 2017; Kulkarni 2020). Of greatest importance to this paper, the DM can be used to infer the electron column density of the diffuse baryons along

a sightline through the CGM independent of their physical condition.

FRBs are a promising tool for probing diffuse matter, especially for baryons in the warm ionized phase, which is barely traceable through self-emission and absorption spectra (McQuinn 2014; Prochaska & Zheng 2019; Connor & Ravi 2022; Wu & McQuinn 2023). While previous studies have demonstrated the utility of FRBs for probing the cosmic distribution of baryons (Prochaska & Zheng 2019; Macquart et al. 2020; Khrykin et al. 2024b), these analyses have focused on statistical inferences over large, diverse halo populations.

In contrast, Anna-Thomas et al. (2025) used two localized FRBs with sightlines passing through the inner M31 halo ($R_\perp \lesssim 0.1 r_{\text{vir}}$) to estimate DM contributions of $\sim 9\text{--}145 \text{ pc cm}^{-3}$ and $\sim 28\text{--}286 \text{ pc cm}^{-3}$ along individual sightlines, providing constraints on M31’s CGM from FRBs.

In this work, we examine the properties of a single, well-characterized system, M31, whose large angular extent and proximity to the Milky Way place it in the path of multiple FRB sightlines. We construct a sample of FRBs that intersect the M31 halo and statistically compare their DMs to a control sample of non-intersecting FRBs. From the inferred DM associated with the M31 halo, we constrain the total ionized gas content of its CGM and, by extension, its baryonic mass.

This paper is structured as follows: In Section 2, we describe the methods used for modelling the M31 halo, data selection, and construction of a control sample. In Section 3, we set out the analysis techniques, sandboxing and validating the methods utilising simulated samples of FRBs. In Section 4, we apply the developed methodology to the real data and report the results. In Section 5, we discuss the implications of our results as they pertain to the total mass of the baryons in the CGM of M31 and the fraction of baryons retained by the halo. We compare our methodology with other probes used to study the CGM of M31, and also discuss possible systematics and the potential for future work to attain better constraints. Finally, we summarise our conclusions in Section 6.

2. METHODOLOGY

2.1. Modeling M31’s Halo

We adopt the following physical parameters for the M31 system, summarized in Table 1.

Distance and Position: We adopt a distance to M31 of 752 kpc (Riess et al. 2012) and place the projected center of the halo at Galactic coordinates $(l, b) = (121.17^\circ, -21.57^\circ)$ (Courteau et al. 2011).

Halo Mass: We adopt a total halo mass of $M_{\text{halo}} = 1.5 \times 10^{12} M_\odot$, as estimated by van der Marel et al. (2012) using Local Group kinematics. This is consistent with constraints from M31’s rotation curve and satellite dynamics (Patel & Mandel 2023).

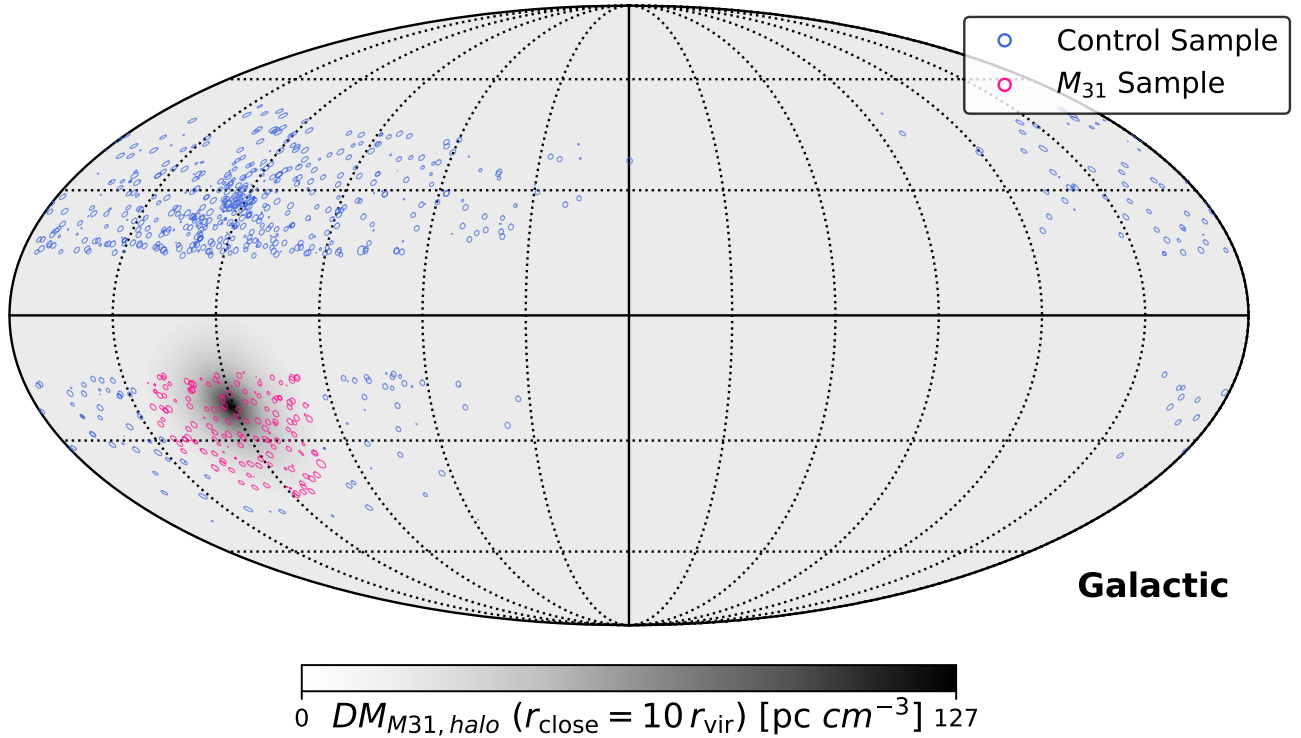


Figure 1. Skymap of the final analysis catalog (built from FRBs in CHIME/FRB Catalog 2 (CHIME/FRB Collaboration et al. 2026)) showing the locations of 171 FRBs intersecting M31’s halo (within r_{vir}) and the corresponding control sample of 684 FRBs. The ellipse markers represent the $\approx 3\sigma$ localisations of each FRB. The inset in the bottom left region shows the extent of the M31 halo and the predicted $DM_{M31,\text{halo}}$ contribution from a generalized halo model (see Section 2.1.1) with an assumed $r_{\text{close}} = 10.0 r_{\text{vir}}$. The overdensity of detected FRBs at the Celestial North Pole is due to the orientation of CHIME, which is positioned to face North-South and is located in the Northern Hemisphere; therefore, it is always oriented North-South and the North Pole is always in the field of view.

Virial Radius: We define the virial radius using the spherical collapse overdensity for a flat Λ CDM cosmology (Bryan & Norman 1998). The virial overdensity relative to the critical density is

$$\Delta_{\text{vir}} = 18\pi^2 - 82q - 39q^2, \quad (2)$$

where $q \equiv \Omega_\Lambda / [\Omega_\Lambda + \Omega_m(1+z)^3]$ is the dark energy density parameter at redshift z . The virial radius is then

$$r_{\text{vir}} = \left(\frac{3M_{\text{halo}}}{4\pi\Delta_{\text{vir}}\rho_c} \right)^{1/3}, \quad (3)$$

where $\rho_c = 3H_0^2/(8\pi G)$ is the critical density. For our adopted halo mass and $z \approx 0$, this yields $r_{\text{vir}} = 302\text{kpc}$, corresponding to an angular radius of $\approx 23^\circ$ at the distance of M31.

Stellar Mass: The stellar mass of M31 is $M_*^{\text{M31}} = (12 \pm 3) \times 10^{10} M_\odot$ (Tamm et al. 2012), corresponding to $\approx 50\%$ of the cosmic baryonic mass $M_{b,\text{cosmic}} \equiv (\Omega_b/\Omega_m)M_{\text{halo}} \approx 24 \times 10^{10} M_\odot$. This suggests that a substantial fraction of baryons may reside in the CGM.

2.1.1. CGM Density Profile

To model the distribution of ionized gas in M31’s CGM, we employ a generalized halo model that builds on the modified Navarro-Frenk-White (mNFW) profile introduced by Prochaska & Zheng (2019). Our framework addresses a key limitation of standard mNFW models: they lack a mechanism to enforce the cosmic baryon fraction at large radii.

The central insight of our approach is to define the enclosed baryon mass as a modulated fraction of the enclosed dark matter mass:

$$M_b(< r) = g(y) \frac{\Omega_b}{\Omega_m - \Omega_b} M_{\text{dm}}(< r), \quad (4)$$

where $y \equiv cr/r_{\text{vir}}$ is the dimensionless radius scaled by the concentration parameter c , and $g(y)$ is a modulation function satisfying $g(0) = 0$ (baryon depletion in the inner halo due to feedback) and $\lim_{y \rightarrow \infty} g(y) = 1$ (recovery of the cosmic baryon fraction at large radii). This construction guarantees that the enclosed baryon fraction approaches Ω_b/Ω_m asymptotically, regardless of the specific form of $g(y)$.

Table 1. Adopted parameters for the M31 system.

Parameter	Value	Reference
Distance d	752 kpc	Riess et al. (2012)
Galactic (l, b)	$(121.17^\circ, -21.57^\circ)$	Courteau et al. (2011)
Halo mass M_{halo}	$1.5 \times 10^{12} M_\odot$	van der Marel et al. (2012)
Virial radius r_{vir}	302 kpc	Bryan & Norman (1998)
Stellar mass M_*^{M31}	$(12 \pm 3) \times 10^{10} M_\odot$	Tamm et al. (2012)
Cosmic baryon mass $M_{b,\text{cosmic}}$	$2.4 \times 10^{11} M_\odot$	Derived from Ω_b/Ω_m

We parameterize $g(y)$ using a hyperbolic tangent function:

$$g(y) = \tanh\left(\frac{y}{y_{\text{out}}}\right), \quad (5)$$

where the scale parameter y_{out} is related to a physically motivated *closure radius* $r_{\text{close}} = k r_{\text{vir}}$ at which the enclosed baryon fraction reaches the cosmic mean (Sorini et al. 2022; Ayromlou et al. 2023). The parameter k thus controls the radial extent of baryon redistribution relative to the virial radius.

The baryon density profile derived from Equation (4) takes the form:

$$\rho_b(y) = \frac{\Omega_b}{\Omega_m - \Omega_b} \rho_{\text{dm}}^0 \left[\frac{g(y)}{y(1+y)^2} + \frac{1}{y^2} \frac{dg}{dy} \left(\ln(1+y) - \frac{y}{1+y} \right) \right], \quad (6)$$

where ρ_{dm}^0 is the NFW normalization density. The first term represents a modulated NFW profile, while the second term ensures proper asymptotic behavior. The full derivation and discussion of model properties will be provided by Simha et al (in prep).

For our fiducial analysis, following Prochaska & Zheng (2019), we adopt $c = 7.67$ for the NFW concentration parameter. We treat k as a free parameter to be constrained by the FRB observations, exploring values in the range $k = 0.5\text{--}30$ corresponding to closure radii from $0.5 r_{\text{vir}}$ to $30 r_{\text{vir}}$. Table 2 summarizes the model parameters.

Table 2. Parameters of the generalized halo model.

Parameter	Value/Range	Description
c	7.67	NFW concentration parameter
k	0.5–30	Closure radius in units of r_{vir}
Ω_b/Ω_m	0.158	Cosmic baryon fraction

2.1.2. Dispersion Measure from M31's Halo

The dispersion measure contribution from M31's CGM at impact parameter R_\perp is obtained by integrating the free

electron density along the line of sight:

$$\text{DM}_{\text{M31,halo}}(R_\perp) = 2 \int_0^{\sqrt{r_{\text{close}}^2 - R_\perp^2}} n_e(\ell) d\ell, \quad (7)$$

where the factor of 2 accounts for both the near and far sides of the halo, and the integration extends to the closure radius $r_{\text{close}} = k r_{\text{vir}}$.

The electron density is related to the baryonic mass density by:

$$n_e = \frac{\mu_e \rho_b}{m_p \mu_H}, \quad (8)$$

where m_p is the proton mass, $\mu_H = 1.3$ is the mean mass per hydrogen atom (accounting for helium), and $\mu_e = 1.167$ is the number of free electrons per baryon assuming full ionization with primordial helium abundance.

These predicted DM contributions are comparable to the scatter in the FRB DM distribution from other sources (e.g., $\text{DM}_{\text{cosmic}}$ and DM_{host} ; see Section 2.3), motivating the statistical approach developed in Section 3.

2.2. FRB Selection

Our analysis utilizes the CHIME/FRB Catalog 2 (CHIME/FRB Collaboration et al. 2026), which includes 3641 unique FRB sources detected by the CHIME experiment, as described by CHIME/FRB Collaboration et al. (2018). Briefly, CHIME is a cylindrical radio transit telescope located near Penticton, British Columbia. The telescope comprises four semicylindrical paraboloid reflectors, each measuring 20 meters in diameter and 100 meters in length, and is equipped with 256 dual-polarization feeds. Using a robust backend system, the CHIME/FRB project processes real-time data to search for FRBs within its field of view. CHIME detects 2–3 FRBs per day on average (Joseph et al. 2021), an exceptionally high detection rate made possible by its large field of view, wide bandwidth, high sensitivity, and powerful correlator.

Cook et al. (2024) model the sensitivity of CHIME/FRB as a function of source declination (δ), parameterized by the relation $\cos^t(\phi - \delta)$, where ϕ is the telescope's geographic latitude and t is empirically fit using CHIME/FRBs beam

model as a prior¹. They find $\iota \approx 1.43$, indicating a steep decline in sensitivity with increasing zenith angle. The peak sensitivity occurs near $\delta \approx 49.3^\circ$, placing M31 (at $\delta \approx 41.3^\circ$) close to this maximum.

An event is deemed extragalactic if its DM_{FRB} exceeds the maximum Galactic estimate for that sightline ($DM_{\text{MW,ISM}}$) predicted by models (Cordes & Lazio 2002; Yao et al. 2017) by at least 5σ . Catalog 2 encompasses all bursts detected between 25 July 2018 and 15 September 2023, including 536 bursts from CHIME/FRB Catalog 1 (CHIME/Pulsar Collaboration et al. 2021). In our analysis, we include all non-repeating bursts and the first burst from each apparent repeater in Catalog 2; using the first burst from repeaters avoids double-counting baryons along the same sightline, while selecting the first burst ensures we use detections with the highest signal-to-noise ratio threshold (Fonseca et al. 2020; Pleunis et al. 2021). We have excluded 13 FRBs detected during commissioning and deemed unreliable for statistical analysis. For the sky positions of the FRBs, we used the header localization positions found in the catalog. These positions come with an uncertainty of approximately $\approx 0.2 \times 0.2 \text{ deg}^2$ at a 1σ confidence. Compared to the M31 halo, which spans 30 deg , we can safely ignore the uncertainties in the FRB positions (see Figure 1). The catalog contains 3469 sightlines, with 275 traversing the M31 halo defined by r_{vir} .

2.3. Dispersion Measures

For each FRB, we adopt the dispersion measure obtained by the FITBURST algorithm (for details, see CHIME/Pulsar Collaboration et al. 2021), DM_{FRB} . The observed DM_{FRB} includes all components along the sightline, as described by Equation 9.

$$DM_{\text{FRB}} = DM_{\text{MW,ISM}} + DM_{\text{MW,halo}} + DM_{\text{cosmic}} + DM_{\text{host}} \quad (9)$$

which is the combined contribution from the Milky Way’s interstellar medium ($DM_{\text{MW,ISM}}$), the contribution from the Milky Way halo ($DM_{\text{MW,halo}}$), and the contributions from the cosmic web (DM_{cosmic}) and the FRB host galaxy DM_{host} . Both of these latter components are functions of the FRB redshift, z_{FRB} . In this paper, we define the Milky Way-ISM subtracted DM:

$$DM_{\text{ext}} \equiv DM_{\text{FRB}} - DM_{\text{MW,ISM}} \quad (10)$$

with $DM_{\text{MW,ISM}}$ values given by the NE2001 model (Cordes & Lazio 2002). For sightlines that intersect the M31 halo, DM_{ext} will include the contribution from $DM_{\text{M31,halo}}$ whereas we expect a negligible contribution at separations greater than r_{vir} .

This enables us to perform a differential experiment between a sample of M31 FRBs and a matched control sample.

To minimize uncertainties arising from $DM_{\text{MW,ISM}}$, we excluded all FRBs located near the Galactic plane, specifically those within $\pm 5^\circ$ of the Galactic plane ($b = 0^\circ$). Additionally, we removed all sightlines with $DM_{\text{MW,ISM}} > 100 \text{ pc cm}^{-3}$. Throughout this paper, we shall refer to FRBs whose sightlines intersect the M31 halo within the virial radius, which is $\approx 23^\circ$ from the center of M31, as M31 FRBs. There are 171 FRBs satisfying the above cuts; these comprise the final sample of M31 FRBs.

X-ray emission and absorption measurements firmly establish the presence of a hot, extended Milky Way halo (Bregman & Lloyd-Davies 2007). However, its density structure and total column remain uncertain. Keating & Pen (2020) compared a suite of gas-density profiles with soft X-ray constraints and showed that the resulting $DM_{\text{MW,halo}}$ spans more than an order of magnitude across physically allowed models. Because of this large model-dependent uncertainty, and the additional anisotropy introduced by our off-center position in the Galaxy, we do not attempt to model $DM_{\text{MW,halo}}$ explicitly. Instead, our experiment is differential: by comparing sightlines that intersect the M31 halo with a declination- and latitude-matched control sample, we effectively remove the mean Milky Way halo contribution and isolate the $DM_{\text{M31,halo}}$ associated with M31.

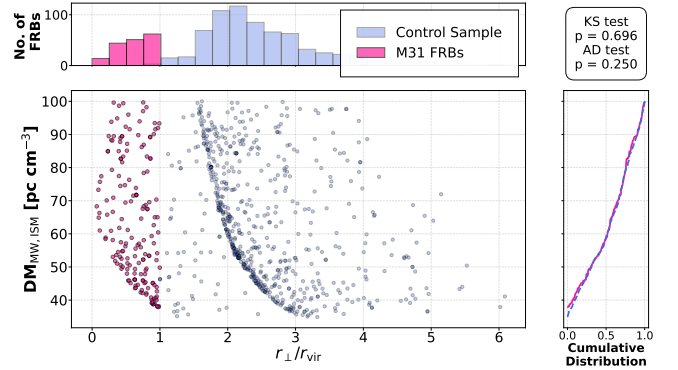


Figure 2. Top: Number of FRBs in the M31 (pink) and control (blue) samples as a function of sightline impact-parameter from M31 (R_{\perp}). By design, the number of FRBs in the control sample is four times that of M31 sightlines. Lower left: A comparison of the $DM_{\text{MW,ISM}}$ values in R_{\perp} space between the M31 sightlines and those for the control sample. Lower right: A CDF plot comparing the $DM_{\text{MW,ISM}}$ distributions of the control sample vs the M31 sightlines, indicating they were drawn from the same distribution. We performed an Anderson-Darling (AD) test to compare the control sample vs the M31 FRBs sample in $DM_{\text{MW,ISM}}$. The AD test returned a p -value of 0.25, indicating we cannot reject the null hypothesis that the two are from the same distribution.

¹ Available at <https://chime-frb-open-data.github.io/beam-model/>

2.4. Control Sample

An important challenge in isolating $DM_{M31, \text{halo}}$ is the need to properly account for uncertainty incurred by line-of-sight variations in $DM_{MW, \text{ISM}}$. Since the ISM structure is not uniform across the sky, particularly at low Galactic latitudes, spatially correlated fluctuations in $DM_{MW, \text{ISM}}$ can bias inferences drawn from comparing FRBs intersecting M31 with those that do not. This is especially problematic when using a global or averaged model of the Milky Way contribution. To address this, we construct a control sample of non-M31 FRBs that are matched in key sky properties to the M31 sightlines, specifically in $DM_{MW, \text{ISM}}$ and Galactic latitude, thereby minimizing differential systematics. This strategy allows us to attribute observed DM differences more confidently to the CGM of M31.

The control sample is built from the set of FRBs beyond M31’s virial radius as follows. For each FRB in the M31 sample, we select corresponding FRBs from the sightlines away from the M31 halo that satisfies the following criteria:

- The $DM_{MW, \text{ISM}}$ values must match within $\pm 3 \text{ pc cm}^{-3}$. This minimizes the statistical difference in the $DM_{MW, \text{ISM}}$ distribution.
- The Galactic latitudes must match within $|\delta b| < 5 \text{ deg}$. This is intended to further reduce differences in the Galactic ISM contributions to the two samples. Since the $DM_{MW, \text{ISM}}$ distribution in Galactic latitude is expected to be symmetric except for individual HII regions, FRBs in a similar Galactic latitude in the Northern hemisphere also satisfy this condition. Indeed, Figure 1 shows that the control sample is biased towards the Northern hemisphere, a potential systematic we discuss in Section 5.3.

We repeat the above procedure for all M31 FRBs while ensuring each M31 FRB has the same number of FRBs from non-M31 sightlines associated with it so as not to alter the entire sample’s PDF. With the above criteria, each M31 FRB could be matched to at least 4 non-M31 FRBs; these 684 FRBs comprise the control sample.

To validate the similarity between the DM_{ISM} distributions of the final analysis samples, we performed a two-sample Anderson-Darling (AD) test. The AD test yielded a p -value of 0.25, indicating that the M31 and non-M31 DM_{ISM} samples are statistically consistent with being drawn from the same underlying distribution. Figure 2 shows the resulting CDF plot of the control sample vs. M31 FRBs and illustrates each sample’s sizes; the control sample size is four times larger than the M31 FRBs sample, ensuring significant statistical power for assessing the average sightline away from M31. Figure 2 also shows the distribution of the two samples as a function of distance from the center of M31, reported as the fraction of the impact parameter to the virial radius of M31 (see Section 2.1).

The distribution of our final analysis catalog in Galactic coordinates is illustrated in Figure 1. The final sample consists of 171 M31 FRBs, along with a control sample of 684 FRBs. Among the M31 sightlines, 58 lie within half the virial radius, while 113 lie in the outer half. Only four sightlines are within 30 kpc of M31’s center, such that our estimates exclude diffuse and ionized baryons from the M31 disk.

3. ANALYSIS FRAMEWORK

3.1. Sandboxing with Mock FRB Samples

To develop and test our analysis techniques, we construct a “sandbox” of mock FRBs with a known M31 halo contribution to their DMs. The two main ingredients in the mock samples are the sky positions and the DM_{FRB} of the FRBs.

To generate mock sky positions consistent with the spatial distribution of FRBs in CHIME/FRB Catalog 2 (CHIME/FRB Collaboration et al. 2026), we fit a two-dimensional kernel density estimate (KDE) to the joint distribution of right ascension (RA) and declination (Dec) from the full catalog (prior to any selection cuts). We then draw mock (RA, Dec) pairs from this KDE, yielding sky positions that faithfully reproduce the correlated spatial structure of the observed FRB population, including CHIME’s declination-dependent sensitivity.

Similar to real data, we assume the $DM_{MW, \text{ISM}}$ values for the mock sightlines follow the NE2001 model and assign them according to their position on the sky. To speed up the calculation of $DM_{MW, \text{ISM}}$, we constructed a HEALPix map (resolution $\approx 0.01 \text{ deg}$) of its values across the sky. For each mock FRB, the corresponding $DM_{MW, \text{ISM}}$ is assigned by querying this map at the generated sky position.

We generate mock values of DM_{FRB} using inverse transform sampling. We construct a cumulative distribution function (CDF) of the DM_{FRB} distribution from the real data, draw uniform random variates from the interval $[0, 1]$, and interpolate through the CDF to obtain mock DM_{FRB} values. The extragalactic contribution is then computed as $DM_{\text{ext}} = DM_{\text{FRB}} - DM_{MW, \text{ISM}}$. We then proceed to perform $DM_{MW, \text{ISM}}$ and Galactic latitude cuts (see Sections 2.2 and 2.4) to make the final mock sample for analysis.

From the surviving set of FRBs that intersect M31, we generate a control sample of 4 FRBs per M31 FRB. At this stage, the mock M31 sightlines and control sample are drawn from the same underlying DM_{ext} distribution, but random sampling fluctuations can introduce a spurious offset between their weighted means. To ensure an unbiased baseline before injecting a mock signal, we randomly replace the DM_{ext} values for the M31 sightlines with values drawn from the control sample until δDM (the difference in the weighted mean DM_{ext} between the M31 and control samples; defined formally in Section 3.3) is less than $10^{-3} \text{ pc cm}^{-3}$ (i.e., negligible compared to the expected halo signal of $\mathcal{O}(50\text{--}200) \text{ pc cm}^{-3}$ (e.g., Prochaska & Zheng 2019; Connor & Ravi 2022; Wu & Mc-

Quinn 2023)), where δDM serves as our primary estimator of the M31 halo’s DM contribution. This procedure guarantees that any non-zero δDM measured after signal injection is attributable solely to the injected M31 contribution, rather than to pre-existing statistical fluctuations between the samples. To the M31 FRB sightlines, we then add the $\text{DM}_{\text{M31,halo}}$ signal we hope to extract; we assume an M31 CGM described by the generalized halo model defined in Section 2.1.1.

We created mock samples of varying sizes to test our methodology. Our primary mock sample contains 3,000 FRBs (henceforth mock_{3000}), including 246 M31 sightlines, mirroring the sample size of the CHIME/FRB Catalog 2. After applying the data selection criteria, this yields 182 mock M31 FRBs. To assess how our methodology would perform with larger samples and to evaluate its predictive power, we also created additional samples with $\approx 20,000$ and $500,000$ FRBs (see Section 5.4 for further discussion).

3.2. Unweighted Comparison

As a first test on whether the DM_{ext} values of the mock M31 FRBs differ statistically from the mock control sample, we may compare their cumulative distribution functions (CDFs), shown in Figure 3. We obtain these CDFs from the mock_{3000} sample, after applying Galactic plane and DM_{MWISM} cuts. The sample contained 186 M31 FRBs (mirroring the 177 M31 FRBs in the real sample). The blue curve illustrates the CDF of the DM_{ext} of the control sample, while the magenta curve represents the CDF of the DM_{ext} of M31 FRBs, which includes a mock signal added as described in Section 3.1. To assess whether the apparent excess in DM_{ext} values for the mock M31 FRBs is statistically significant, we perform a two-sample Anderson-Darling (AD) test on the two CDFs. The null hypothesis assumes that both samples are drawn from the same underlying distribution. Because our M31 and control samples are imbalanced in size, we compute p -values using a permutation test rather than relying on asymptotic distributions. We pool the two samples, randomly partition them into groups matching the original sample sizes, and recompute the test statistic for each of $B = 1,000$ permutations. The p -value is then given by:

$$p = \frac{1 + \sum_{b=1}^B \mathbf{1}[T_b \geq T_{\text{obs}}]}{(B+1)}$$

Here T_{obs} is the AD test statistic computed from the observed samples, T_b is the statistic computed from the b -th random partition of the pooled data, and $\mathbf{1}[T_b \geq T_{\text{obs}}]$ is the indicator function, equal to 1 when the permuted statistic equals or exceeds the observed value and 0 otherwise.

This procedure is used for all AD p -values reported throughout this paper. The AD test yields $p = 0.25$. The test does not detect the injected mock signal at the $p < 0.05$ significance

level, illustrating the challenge of detecting M31’s DM contribution using a simple CDF comparison of the full sample.

The downside to this simple statistical comparison is that one cannot estimate any quantitative difference in DM_{ext} between the two samples. Furthermore, the high-DM events likely include substantial contributions unrelated to M31, reducing sensitivity to a halo signal. This motivates the use of a *weighted mean* approach, as introduced in the following section.

3.3. Weighted Estimator of the M31 Contribution (δDM)

Wu & McQuinn (2023) estimated the DM contribution of the CGM from low-redshift galaxies with masses of $10^{11} - 10^{13} M_{\odot}$ using CHIME/FRB Catalog 1. The sample contained 20–30 FRBs intersecting halos at $< 1 r_{\text{vir}}$, with most FRBs interacting with only one halo. Their analysis introduced a weighted “stacking scheme” to reduce variance and mitigate bias from high-DM FRBs. They then estimated the DM contribution from the CGM of galaxies as the difference in the weighted mean δDM between FRBs with intersecting sightlines and those without.

We adopt the formalism of Wu & McQuinn (2023) for the CGM of M31, defining the average M31 contribution as the difference in the weighted mean between the DM_{ext} of the M31 sightlines and the DM_{ext} of the control sample:

$$\delta\text{DM} = \sum_{i \in \text{M31}} \text{DM}_i \hat{w}(\text{DM}_i) - \sum_{i \in \text{CS}} \text{DM}_i \hat{w}(\text{DM}_i) \quad (11)$$

where the sums run over FRBs in the M31 sample and control sample (CS), respectively. The normalized weights are defined as

$$\hat{w}(\text{DM}_i) = \frac{w(\text{DM}_i)}{\sum_j w(\text{DM}_j)}, \quad (12)$$

where the sum in the denominator runs over all FRBs in the respective sample (M31 or CS), and

$$w(\text{DM}) = e^{-(\text{DM}/\alpha)^\beta} \quad (13)$$

is the unnormalized weighting function with parameters α (a characteristic DM scale) and β (controlling the steepness of the weighting). The normalization ensures that the weights within each sample sum to unity, so that Equation 11 represents the difference between two weighted mean DM values. We use a similar weighting scheme to Wu & McQuinn (2023), downweighting FRBs with high DM_{ext} values, which are more likely to contain large contributions from the intergalactic medium and other intervening halos.

The weighting function assigns greater weight to low-DM sightlines, where the M31 contribution constitutes a larger fraction of the total DM_{ext} . The parameter α sets the DM scale at which the weight drops to $1/e$, effectively defining a soft

cutoff. The parameter β controls how sharply the weights decrease: $\beta = 0$ corresponds to uniform weighting (unweighted mean), while larger β produces steeper cutoffs.

Critically, Equation 11 is an unbiased estimator only when $\beta = 1$ (Wu & McQuinn 2023). For $\beta \neq 1$, the estimator introduces a systematic offset in δDM . We therefore fix $\beta = 1$ throughout our analysis to ensure no systematic offset in our estimates.

The optimal value for α is then a trade-off between choosing lower values, which minimize the variance in δDM , and larger values, which include signal from a larger fraction of the sample. Plausible DM contributions from $10^{12} M_{\odot}$ galaxy halos range over $50\text{--}200 \text{ pc cm}^{-3}$ (e.g., Prochaska & Zheng 2019; Connor & Ravi 2022; Wu & McQuinn 2023). Therefore, we choose to consider values of $\alpha \geq 200 \text{ pc cm}^{-3}$.

To determine the optimal α , we calculated the standard deviation of the distribution of δDM values ($\delta\text{DM}_{\text{STD}}$) for randomly selected FRBs at fixed $\beta = 1$. From our largest mock sample of 500,000 FRBs (see Section 3.1), we randomly selected 200 FRBs, similar to the number of M31 sightlines in our real sample, and then calculated δDM . We repeated this process to create a distribution of 10,000 δDM values for each α and calculated $\delta\text{DM}_{\text{STD}}$. Figure 3 shows how $\delta\text{DM}_{\text{STD}}$ varies with α at $\beta = 1$. The variance increases monotonically with α , rising steeply at low α before flattening at higher values. Small α values ($\lesssim 200 \text{ pc cm}^{-3}$) yield the lowest variance but aggressively downweight most of the sample, potentially discarding genuine M31 signal. We adopt a fiducial value of $\alpha = 300 \text{ pc cm}^{-3}$, which achieves a $\delta\text{DM}_{\text{STD}}$ of $\sim 15 \text{ pc cm}^{-3}$, representing a reduction by a factor of ~ 1.6 compared to the unweighted limit ($\alpha \rightarrow \infty$), while retaining sensitivity to the expected M31 halo contribution. The shaded band in Figure 3 shows that our results are insensitive to small variations in β around unity ($\beta \in [0.8, 1.2]$). We have verified that our main results are not sensitive to this choice of α : varying α within the range $200\text{--}500 \text{ pc cm}^{-3}$ does not significantly change our conclusions. We present an exploration of different α values in Appendix A.

3.4. Mock Estimates of δDM

In this section, we validate our analysis framework using the mock FRB samples described in Section 3.1. We demonstrate that both non-parametric and parametric approaches can successfully recover an injected M31 halo signal. For these tests, we use the mock_{20,000} sample containing approximately 1,000 M31 sightlines after quality cuts, and inject a signal corresponding to the generalized halo model (Section 2.1.1) with a fiducial closure radius of $k = 5.0$ (i.e., $r_{\text{close}} = 5.0 r_{\text{vir}}$). This choice produces DM contributions in the range $\sim 20\text{--}150 \text{ pc cm}^{-3}$ across the halo, consistent with predictions from previous CGM studies (Prochaska & Zheng 2019; Connor & Ravi 2022; Wu & McQuinn 2023).

3.4.1. Non-parametric, Binned δDM Estimation

We first develop a non-parametric approach to estimate the radial DM contribution of M31, denoted $\delta\text{DM}(R_{\perp})$, without assuming a specific functional form for the halo profile. Our method calculates δDM in discrete bins of impact parameter R_{\perp} , constructing matched M31 and control samples for each bin independently. We then compute δDM for each bin using Equation 11 with our fiducial weighting parameters $(\alpha, \beta) = (300 \text{ pc cm}^{-3}, 1)$.

Figure 4 shows the recovered δDM profile from the mock_{20,000} sample divided into five radial bins spanning $0\text{--}1 r_{\text{vir}}$. The data points represent the measured δDM in each bin, with horizontal error bars indicating the bin width and vertical error bars representing the 1σ uncertainty. The magenta shaded region shows the expected scatter from random sky positions (i.e., the null hypothesis of no M31 signal), estimated by repeatedly drawing matched samples from the control population.

Uncertainties in δDM are estimated using a Monte Carlo approach. For each radial bin, we randomly draw the same number of FRBs from the control sample as in the corresponding M31 bin and compute an “off-halo” δDM value using the same estimation procedure. This process is repeated 10,000 times to generate a distribution of off-halo δDM values. As expected, these distributions are approximately Gaussian with a mean near 0 pc cm^{-3} , since the control sample contains no M31 DM contribution by construction. The standard deviation of each distribution is adopted as the 1σ uncertainty for the corresponding δDM measurement.

All five radial bins show significant detections of the injected signal, with the measurements marked by “***” indicating $> 3\sigma$ significance. The recovered profile decreases monotonically with increasing impact parameter, as expected for a centrally concentrated halo. The innermost bin ($R_{\perp} < 0.2 r_{\text{vir}}$) recovers $\delta\text{DM} \approx 150 \text{ pc cm}^{-3}$, while the outermost bin ($0.8 < R_{\perp}/r_{\text{vir}} < 1.0$) yields $\delta\text{DM} \approx 20 \text{ pc cm}^{-3}$, both consistent with the input model predictions (i.e., following the δDM corresponding to a generalised halo profile with $r_{\text{close}} = 10 r_{\text{vir}}$).

This non-parametric method has several advantages: it requires no assumptions about the functional form of the M31 halo profile, and it is flexible with respect to the choice of binning scheme. However, the choice of bin boundaries is arbitrary, and the method requires a sufficiently large number of FRBs per bin to suppress statistical noise. With smaller samples, the inferred δDM values become highly uncertain.

3.4.2. Parametric Modeling of the M31 Halo

We now develop a parametric approach to constrain the closure radius r_{close} of the generalized halo model directly from the FRB data. This method uses all M31 sightlines simultane-

ously, avoiding the information loss inherent in binning, and provides quantitative constraints on the model parameters.

Following the methodology introduced by [Wu & McQuinn \(2023\)](#), we define a goodness-of-fit metric:

$$\xi^2 = \left(\left\{ \sum_{i \in M_{31}} (DM_i - DM_\gamma) w (DM_i - DM_\gamma) \right\} - \overline{DM}_{cs} \right)^2 \quad (14)$$

where $DM_\gamma(R_\perp)$ is the model-predicted $DM_{M31, \text{halo}}$ at impact parameter R_\perp for a given value of r_{close} , DM_i is the observed DM_{ext} for each M31 sightline, \overline{DM}_{cs} is the weighted mean DM of the control sample, and w is the weighting function defined in Equation 13.

To evaluate the model fit, we normalize ξ^2 by its expected value $\langle \xi^2 \rangle$ to obtain $\chi^2 = \xi^2 / \langle \xi^2 \rangle$. The quantity $\langle \xi^2 \rangle$ accounts for the statistical variance expected from sampling fluctuations and is computed empirically: we draw $N = 10,000$ random subsets of size n_{FRB} (the number of M31 sightlines) from the control sample, compute the weighted mean DM for each subset, and calculate the variance of these weighted means relative to the full control sample mean.

Figure 4 shows the χ^2 profile as a function of r_{close} for the $\text{mock}_{20,000}$ sample. The input model used to generate the mock signal is marked by the green diamond at $k = 5.0$. The best-fit value, corresponding to the minimum χ^2 , is $r_{\text{close}} = 5.5 r_{\text{vir}}$ (red star), in excellent agreement with the input. The 1σ and 2σ confidence intervals are estimated from $\Delta\chi^2 = 1$ and $\Delta\chi^2 = 4$, respectively, yielding approximate ranges of $k \approx 3\text{--}8$ (1σ) and $k \approx 1.5\text{--}12$ (2σ).

The parametric best-fit model is overlaid on the non-parametric measurements in Figure 4. The solid blue curve shows the best-fit model ($k = 5.5 r_{\text{vir}}$), while the dashed green curve shows the input model ($k = 5.0$). The orange and gray shaded regions indicate the 1σ and 2σ model uncertainties, respectively. The agreement between the non-parametric binned estimates and the parametric model fit demonstrates the internal consistency of our analysis framework and validates our ability to recover injected halo signals from FRB samples of this size.

Once r_{close} is constrained, the total CGM mass can be derived under the assumptions of the generalized halo model. For a given r_{close} , the enclosed baryon mass within r_{vir} is determined by the model prescription (Equation 4). We defer the application of this framework to the real data to Section 4.

4. RESULTS

We now apply the analysis framework developed and validated on mock samples (Section 3) to the observed CHIME/FRB Catalog 2 data ([CHIME/FRB Collaboration et al. 2026](#)).

4.1. Unweighted Comparison

Figure 5 compares the CDFs of DM_{ext} between the M31 and control FRB samples in the real data. We find that the two distributions are systematically offset for $DM_{\text{ext}} \lesssim 800 \text{ pc cm}^{-3}$, with M31 sightlines exhibiting larger values, before converging at higher DM. Performing a two-sample Anderson-Darling (AD) test on these CDFs, we recover an AD test p -value of 0.16. The test does not detect a statistically significant difference at the $p < 0.05$ level, consistent with our mock analysis (Section 3.2) which showed that the unweighted CDF comparison lacks sensitivity to the expected M31 signal.

As in the mock sample, we infer that the signal from M31 is diluted at high DM_{ext} , noting that $\approx 15\%$ of FRBs have $DM_{\text{ext}} > 1000 \text{ pc cm}^{-3}$. This motivates the weighted estimator introduced in Section 3.3.

4.2. Non-Parametric Estimation of the M31 DM Contribution

Following the methodology validated in Section 3.4.1, we apply our non-parametric weighted estimator to the observed sample of 171 M31 FRBs. The FRBs were divided into two radial bins corresponding to the inner and outer halo: $0\text{--}0.5 r_{\text{vir}}$ and $0.5\text{--}1 r_{\text{vir}}$, containing 58 and 113 FRBs, respectively. While finer binning is possible in principle, the limited sample size would lead to large uncertainties and potentially non-physical (e.g., negative) δDM estimates in sparsely populated bins.

The measured values of δDM for each bin are shown in Figure 6. We find $\delta DM = 5.9\text{--}59.6 \text{ pc cm}^{-3}$ for the inner bin ($0\text{--}0.5 r_{\text{vir}}$) with a signal-to-noise ratio of 1.2, and $\delta DM = 25.7\text{--}64.6 \text{ pc cm}^{-3}$ for the outer bin ($0.5\text{--}1 r_{\text{vir}}$) with a signal-to-noise ratio of 2.3.

In this context, the signal-to-noise ratio is defined as $S/N \equiv \delta DM / \sigma_{\text{rand}}$, where σ_{rand} is the standard deviation of δDM measured along random positions on the sky. The random-sky distribution is constructed by repeating the same measurement procedure on control sightlines that are not associated with M31. The quoted 1σ uncertainties correspond to the dispersion of this Monte Carlo random-sky distribution, as described in Section 3.4.1.

The resulting δDM profile is qualitatively consistent with a halo-associated DM contribution from M31. Both bins yield positive δDM values that lie above the random-sky expectation (magenta shaded region in Figure 6), with the outer bin showing a stronger detection ($\text{SNR} = 2.3$). We also show for comparison the recent measurements by [Anna-Thomas et al. \(2025\)](#) from two localized FRBs with sightlines passing through the inner M31 halo (red diamonds). Their estimates of $\delta DM \approx 60\text{--}145 \text{ pc cm}^{-3}$ at $R_\perp \lesssim 0.1 r_{\text{vir}}$ are consistent with our binned measurements and the parametric model fits described below.

4.3. Constraining r_{close} with Parametric Modeling

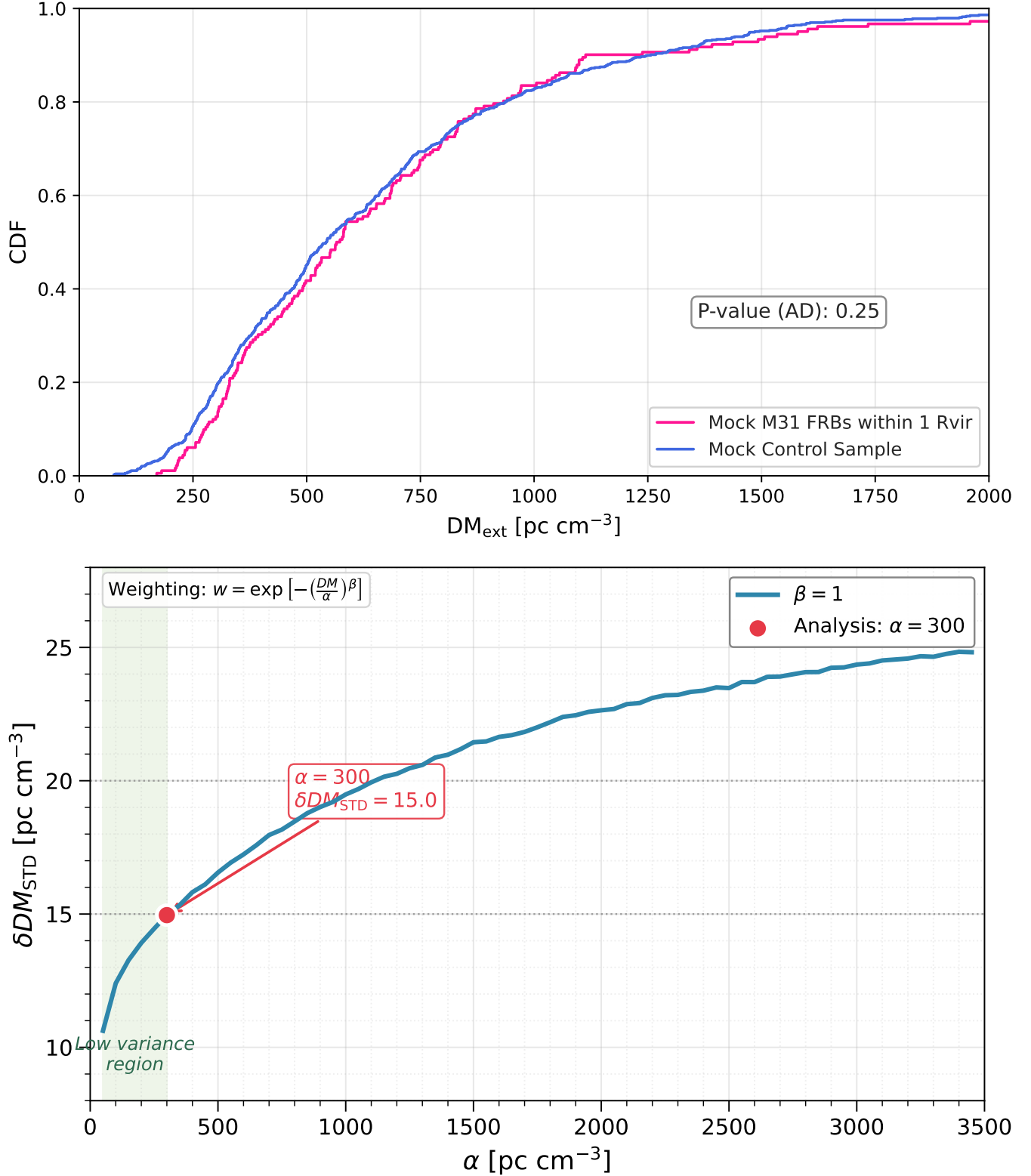


Figure 3. Top: Comparison of the CDFs for the extragalactic DMs DM_{ext} for CHIME/FRBs within 1 virial radius of M31 (magenta) versus the control sample (blue) for our mock₃₀₀₀ sample. The AD test yields $p = 0.25$, indicating no significant difference between the two populations at the $p < 0.05$ level. Note the apparent offset at $DM_{\text{ext}} < 800 \text{ pc cm}^{-3}$ suggesting a non-negligible $DM_{\text{M31,halo}}$ may be retrieved from the lower DM sightlines, which should suffer less contamination from non-M31 contributions. **Bottom:** Standard deviation of the weighted mean difference (δDM_{STD}) as a function of α at fixed $\beta = 1$. The blue curve shows δDM_{STD} computed from 10,000 random draws of 200 FRBs from our mock sample. The green shaded region marks the low-variance regime at small α . The red point indicates our fiducial choice of $\alpha = 300 \text{ pc cm}^{-3}$, which achieves $\delta DM_{\text{STD}} \approx 15 \text{ pc cm}^{-3}$ while retaining sensitivity to plausible M31 halo DM contributions.

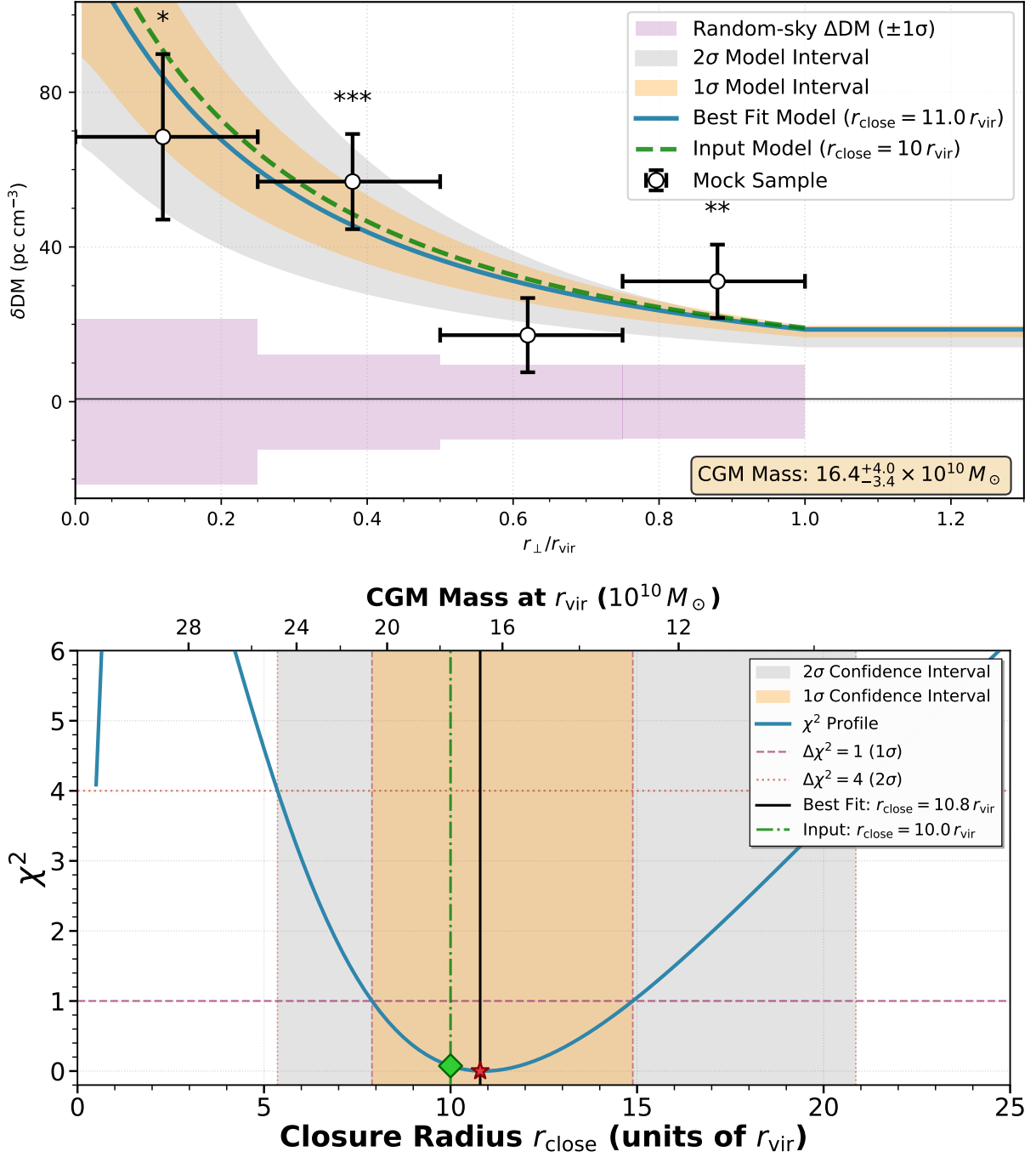


Figure 4. Top: Non-parametric recovery of the injected M31 halo signal from the mock_{20,000} sample with overplotted best fit values from the parametric analysis. Data points show the measured δDM in five radial bins, with vertical error bars indicating 1σ uncertainties estimated via Monte Carlo resampling of the control sample. Horizontal bars indicate bin widths. The magenta shaded region shows the $\pm 1\sigma$ range expected for random sky positions with no M31 signal. All bins show highly significant detections (** indicates $> 2\sigma$, *** indicates $> 3\sigma$). The solid blue curve shows the best-fit parametric model ($r_{\text{close}} \approx 11 r_{\text{vir}}$), with orange (1σ) and gray (2σ) shaded regions indicating model uncertainties. The dashed green curve shows the input model ($r_{\text{close}} = 10 r_{\text{vir}}$). **Bottom:** Parametric constraints on the closure radius r_{close} from the mock_{20,000} sample. The blue curve shows the χ^2 profile as a function of r_{close} (in units of r_{vir}). The horizontal dashed lines mark $\Delta\chi^2 = 1$ and $\Delta\chi^2 = 4$, corresponding to 1σ and 2σ confidence levels. The orange and gray shaded regions indicate the corresponding confidence intervals. The green diamond marks the input model value ($k = 10$), while the red star marks the best-fit value ($k \approx 11$). The close agreement validates our parametric framework.

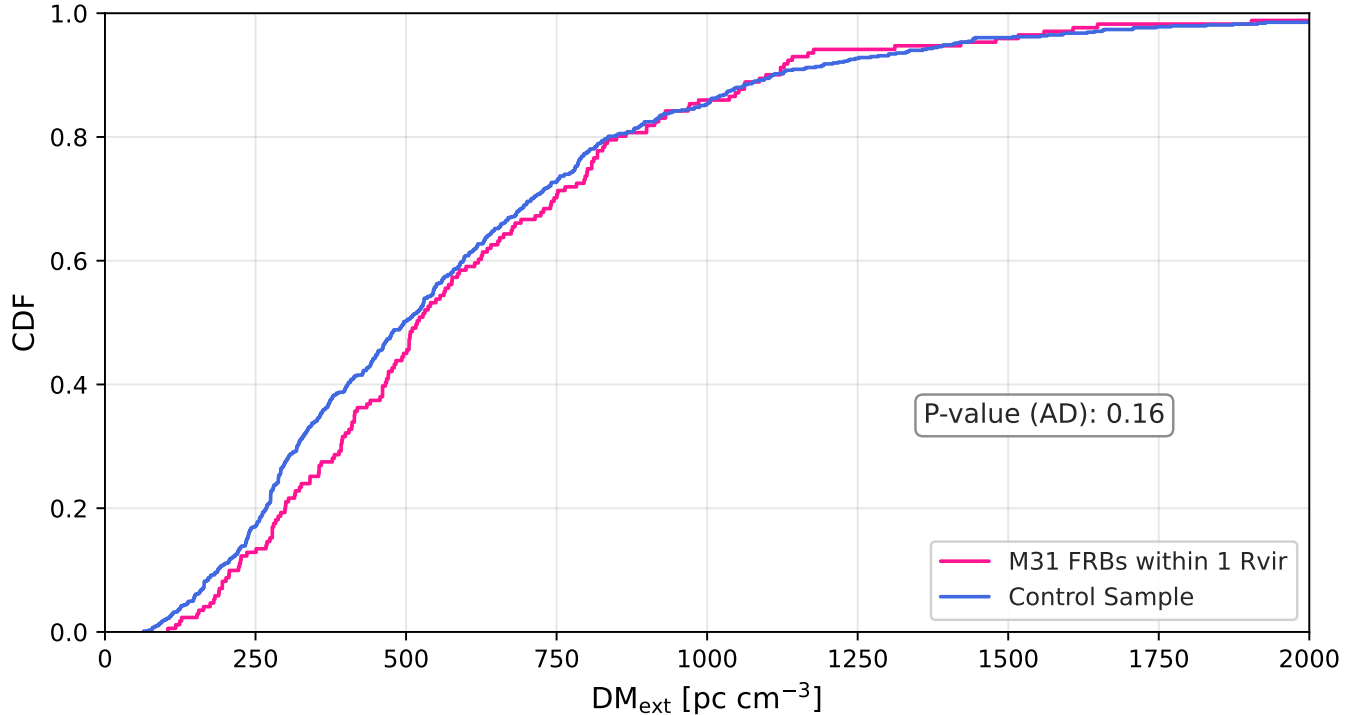


Figure 5. Comparison of the CDFs for the extragalactic DMs DM_{ext} for CHIME/FRBs within $1 r_{\text{vir}}$ of M31 (magenta) versus the control sample (blue) for the observed data. The AD test yields $p = 0.16$, indicating no significant difference between the two populations at the $p < 0.05$ level. Similar to our mock sample (Figure 3), the apparent offset at $DM_{\text{ext}} < 800 \text{ pc cm}^{-3}$ suggests a non-negligible $DM_{\text{M31,halo}}$ may be retrieved from the lower DM sightlines using the weighted estimator.

Our binned measurements of $\delta DM(R_{\perp})$ provide suggestive evidence for an M31 CGM detection. We now employ the parametric methodology developed in Section 3.4.2 to constrain the closure radius r_{close} of the generalized halo model and derive the corresponding CGM mass.

Figure 6 shows the χ^2 profile as a function of r_{close} for the observed data. The best-fit value, corresponding to the minimum χ^2 , is $r_{\text{close}} = 9.2 r_{\text{vir}}$ (red star). The 1σ confidence interval, estimated from $\Delta\chi^2 = 1$, spans $r_{\text{close}} = 4.3\text{--}19.2 r_{\text{vir}}$ (orange shaded region). The 2σ interval ($\Delta\chi^2 = 4$) is well constrained on the lower- r_{close} side, yielding $r_{\text{close}} = 1.4 r_{\text{vir}}$, which corresponds to a 2σ lower limit on $M_{b,\text{halo}}$. However, toward larger r_{close} values the χ^2 profile flattens within the explored parameter range, and thus our analysis does not provide an upper 2σ bound given the adopted limits on r_{close} (gray shaded region).

The upper axis of Figure 6 shows the corresponding CGM mass enclosed within r_{vir} , derived from the generalized halo model prescription (Equation 4). The best-fit closure radius of $r_{\text{close}} = 9.2$ corresponds to a CGM mass of $M_{b,\text{halo}} = 18.6^{+7.9}_{-8.4} \times 10^{10} M_{\odot}$. This estimate represents the total ionized gas mass in the M31 halo within the virial radius, under the assumptions of our generalized halo model with full ionization and primordial helium abundance.

The best-fit parametric model is overlaid on the non-parametric measurements in Figure 6. The solid blue curve shows the model prediction for $r_{\text{close}} = 9.2 r_{\text{vir}}$, while the orange and gray shaded regions indicate the 1σ and 2σ model uncertainties, respectively.

We note that the χ^2 profile is asymmetric, with a steeper rise toward small r_{close} values (concentrated halos) than toward large r_{close} values (extended halos). This reflects the fact that highly concentrated models predict large δDM values in the inner halo that are inconsistent with our measurements, while extended models with $r_{\text{close}} \gtrsim 10 r_{\text{vir}}$ produce relatively flat δDM profiles that remain marginally consistent with the data. Future observations with larger FRB samples will be needed to break this degeneracy and provide tighter constraints on the halo structure. Indeed, the χ^2 profile does not reach $\Delta\chi^2 = 4$ on the high- r_{close} side within the explored parameter range, leaving the 2σ upper limit on the closure radius (and correspondingly, the 2σ lower limit on $M_{b,\text{halo}}$) formally unconstrained. Future observations with larger FRB samples will be needed to break this degeneracy and provide tighter constraints on the halo structure.

5. DISCUSSION

In this section, we discuss the implications of our results for the baryon content of M31, compare with previous CGM

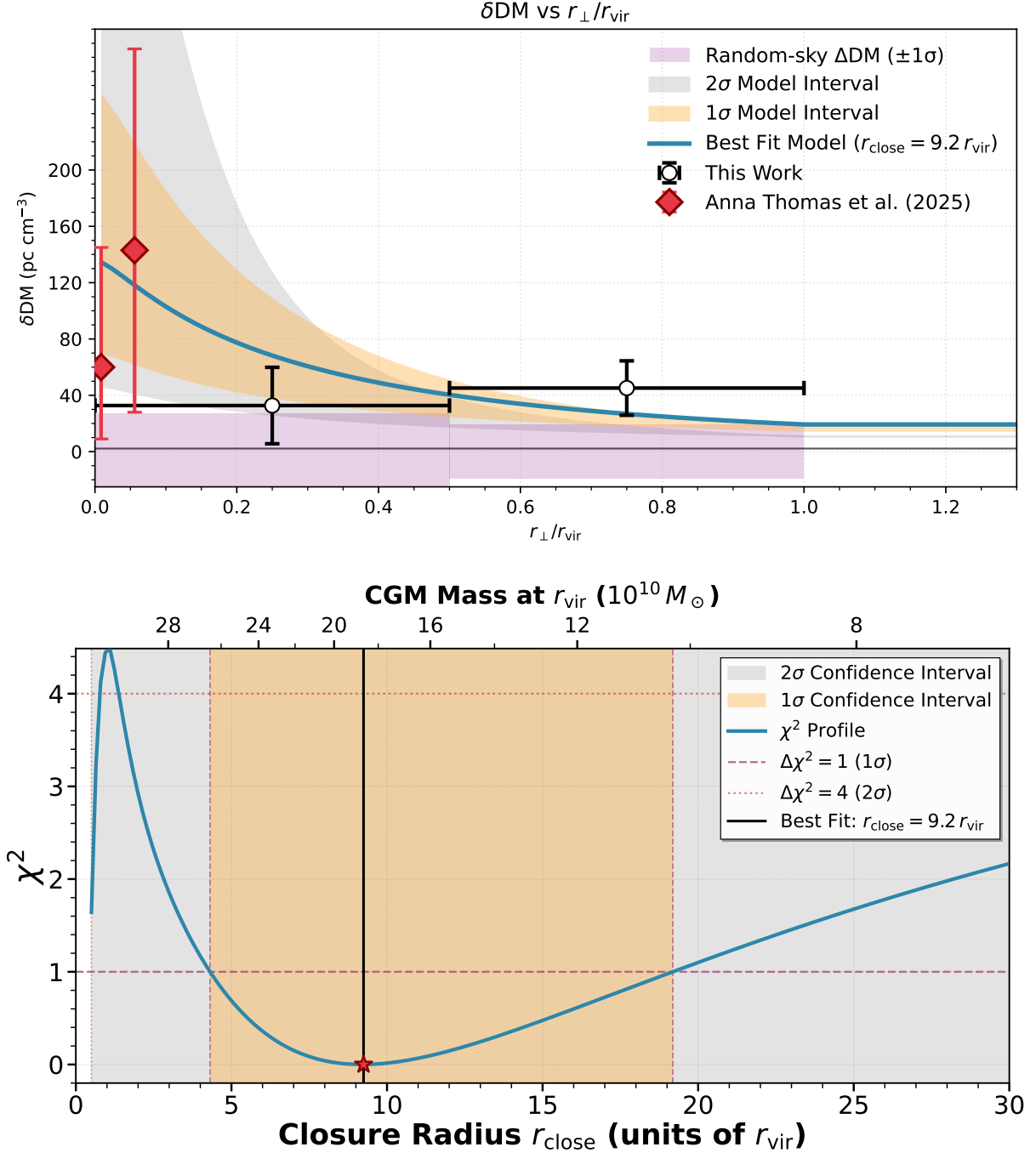


Figure 6. Top: Non-parametric estimation of the M31 halo DM contribution from the observed CHIME/FRB Catalog 2 data. Open circles show our measurements of δDM in two radial bins ($0-0.5 r_{\text{vir}}$ and $0.5-1 r_{\text{vir}}$), with vertical error bars indicating 1σ uncertainties and horizontal bars indicating bin widths. Red diamonds show independent measurements from [Anna-Thomas et al. \(2025\)](#) based on two localized FRBs passing through the inner M31 halo. The magenta shaded region shows the $\pm 1\sigma$ range expected for random sky positions with no M31 signal. The solid blue curve shows the best-fit parametric model ($r_{\text{close}} = 9.2 r_{\text{vir}}$), with orange (1σ) and gray (2σ) shaded regions indicating model uncertainties from the χ^2 analysis (bottom panel). **Bottom:** Parametric constraints on the closure radius r_{close} from the observed CHIME/FRB data ([CHIME/FRB Collaboration et al. 2026](#)). The blue curve shows the χ^2 profile as a function of r_{close} (bottom axis, in units of r_{vir}). The top axis shows the corresponding CGM mass enclosed within r_{vir} , derived from the generalized halo model. Horizontal dashed lines mark $\Delta\chi^2 = 1$ and $\Delta\chi^2 = 4$, corresponding to 1σ and 2σ confidence levels. The orange and gray shaded regions indicate the corresponding confidence intervals. The red star marks the best-fit value $r_{\text{close}} = 9.2 r_{\text{vir}}$, corresponding to a CGM mass of $M_{b,\text{halo}} = 18.6_{-8.4}^{+7.9} \times 10^{10} M_{\odot}$.

measurements, address potential systematic uncertainties, and consider prospects for future FRB surveys.

5.1. Total Mass of Baryons in M31

Studies of the CGM indicate that for L^* galaxies with halo masses $\sim 10^{12} M_\odot$, typically less than 25% of the cosmic baryonic mass $M_{b,\text{cosmic}}$ of the halo resides in the stellar disk (e.g., Behroozi et al. 2019). This implies that $\approx 75\%$ of $M_{b,\text{cosmic}}$ is “missing” from our view. Either the gas is too diffuse for detection with our facilities, or a substantial fraction of baryons was expelled beyond the virial radius into the IGM by feedback processes (e.g., Bregman 2007; McQuinn 2016; Khrykin et al. 2024a). This inefficiency in baryon retention is a key challenge in galaxy formation theory. Kravtsov et al. (2018) suggest that most galaxies are inefficient at converting their available baryons into stars, with Milky Way-mass halos typically locking less than 20% of their expected baryon budget in stars and ISM. This inefficiency is shaped by a combination of physical processes, including supernova and AGN feedback, galactic winds, and halo-scale heating, which prevent baryons from reaching or cooling within the ISM (see, for example, the review by Chen & Zahedy 2024). The CGM acts as a dynamic reservoir where these processes leave observable imprints.

With this context in mind, we consider a baryonic census of M31. Remarkably, assuming a halo mass of $M_{\text{halo}} = 1.5 \times 10^{12} M_\odot$ (van der Marel et al. 2012), M31 appears to host a higher-than-typical baryonic fraction in stars and inter-stellar Medium (ISM), compared to other L^* systems. This raises the possibility that M31 is unusually efficient at retaining or re-accreting its baryons. An independent measurement of the total CGM mass is therefore essential to understanding whether M31 is truly atypical or simply under-observed in its diffuse gas phases.

Adopting $M_{\text{halo}} = 1.5 \times 10^{12} M_\odot$ for the total mass of M31, its cosmic baryonic mass corresponds to $M_{b,\text{cosmic}} \approx 10^{11.4} M_\odot$. Figure 7 examines estimates for the major baryonic components of M31, including our own. Measurements of the disk by Tamm et al. (2012) estimate a stellar mass of $(12 \pm 3) \times 10^{10} M_\odot$ (including the bulge). This suggests that the M31 disk corresponds to $\approx 50\%$ of $M_{b,\text{cosmic}}$, notably higher than typical L^* galaxies.

Measurements from Lehner et al. (2025) infer a mass of $\approx 1.88 \pm 1.02 \times 10^9 M_\odot$ and $\approx 3.76 \pm 2.04 \times 10^{10} M_\odot$ for the cool and warm-hot phases of the M31 halo, respectively. It must be noted that the cool and warm-hot mass estimates quoted here assume a metallicity of $Z = 0.3 Z_\odot$ for both phases of the CGM, and UV studies are not sensitive to the hot phase.

Our estimate for the total CGM mass from the FRB experiment is $M_{b,\text{halo}} = 18.6_{-8.4}^{+7.9} \times 10^{10} M_\odot$ (Section 4.3). When expressed as a fraction of $M_{b,\text{cosmic}}$, this corresponds to $\approx 100_{-35}^{+22}\%$ of the expected baryonic content within r_{vir} . When

combined with the stellar disk mass, the total baryonic mass would exceed $M_{b,\text{cosmic}}$ at the 1σ level (Figure 7).

If the combined CGM + disk mass is accurate, this would imply that M31’s total baryon content approaches or exceeds the fraction predicted by Λ CDM, potentially pointing to ongoing IGM accretion or underestimated systematics in our measurement. It supports the growing evidence that the “missing baryons” in L^* halos may reside in hot, diffuse gas extending to large radii. In contrast, simulation results from the SIMBA suite by Khrykin et al. (2024a) suggest that only a small fraction of the ionized baryons are in the CGM, which is in agreement with the combined mass of baryons in the cool and warm-hot CGM from the UV absorption studies (Lehner et al. 2025). Nevertheless, our results highlight the potential of FRBs to help close the gap in accounting for the diffuse and otherwise difficult-to-detect baryons in the CGM of galaxies.

Figure 7 shows our CGM mass estimate in comparison with other probes of M31’s diffuse gas content. Absorption-line measurements toward background quasars (Lehner et al. 2025) and gamma-ray observations (Zhang et al. 2021) yield relatively low estimates of the halo baryon content, suggesting a significant baryon deficit. We also illustrate an upper limit derived from the hot-bridge structure between the M31 and Milky Way halos, inferred from a combination of X-ray and SZ-effect measurements (Qu et al. 2021). Our FRB-based measurement of $M_{b,\text{halo}} = 18.6_{-8.4}^{+7.9} \times 10^{10} M_\odot$ lies between these previous estimates: it is consistent with the AMIGA lower bounds from Lehner et al. (2025) and the hot-bridge upper limit from Qu et al. (2021), but is in tension with the higher upper bound reported by Zhang et al. (2021). This discrepancy may be attributed to significant uncertainties in the gamma-ray intensity and the adopted cosmic-ray diffusion coefficient in the M31 halo. These results demonstrate that FRBs offer a powerful, independent probe of the ionized CGM, capable of placing competitive constraints on its total baryonic content.

5.2. Comparison with Other DM Estimates for Galaxy Halos

In our analysis, we estimated δDM to be $5.9\text{--}59.6 \text{ pc cm}^{-3}$ and $25.7\text{--}64.6 \text{ pc cm}^{-3}$ with signal-to-noise ratios of 1.2 and 2.3 for the two radial bins spanning $0\text{--}0.5 r_{\text{vir}}$ ($\approx 0\text{--}151 \text{ kpc}$) and $0.5\text{--}1 r_{\text{vir}}$ ($\approx 151\text{--}302 \text{ kpc}$), respectively.

Connor & Ravi (2022) used a sample of 474 non-repeating FRBs from the CHIME/FRB catalog to estimate the DM contribution of Galactic halos. They compared the sightlines of the FRBs with galactic halos $< 40 \text{ Mpc}$ from the Gravitational Wave Galaxy Catalog (GWGC). Of the 474 FRBs, 26 intersected galactic halos at impact parameters ranging over $75\text{--}300 \text{ kpc}$. Using the jackknife and Student t -test methods without applying any weighting schemes, they estimate a DM contribution $> 90 \text{ pc cm}^{-3}$ at a 95% confidence limit.

However, from 12 sightlines that intersect the M31 halo, they found no statistically significant DM contribution.

Wu & McQuinn (2023) employed a weighted stacking method on the same sample of 474 FRBs. Using a sample of galaxies at < 80 Mpc, they measure a DM contribution ranging over $20\text{--}50\text{ pc cm}^{-3}$ from galactic halos with masses $10^{12}\text{--}10^{13} M_{\odot}$ (similar to M31) to $1\sigma\text{--}2\sigma$ within $0\text{--}1 r_{\text{vir}}$ of the galactic centers.

Most recent measurements by Anna-Thomas et al. (2025) found that the M31 halo contributes $9\text{--}145\text{ pc cm}^{-3}$ along the sightline of FRB20230903A and $28\text{--}286\text{ pc cm}^{-3}$ along the sightline of FRB20230506C. These localized FRB measurements probe the inner M31 halo ($R_{\perp} \lesssim 0.1 r_{\text{vir}}$) and are shown in Figure 6 for comparison with our binned estimates. The consistency between our statistical analysis and these independent single-sightline measurements lends confidence to both approaches.

Our measurements on M31 are consistent with those of Wu & McQuinn (2023) and Anna-Thomas et al. (2025), suggesting that halos of similar masses will have similar DM contributions. This serves as evidence of the existence of a massive galactic halo around M31, also illustrating the potential of FRBs to be used for estimating the masses of galactic halos. With larger samples, FRBs can be used to estimate the masses of other nearby halos and structures, such as M87 and the Coma Cluster.

5.3. Systematics

Before concluding, we emphasize several sources of potential systematic uncertainty that could affect our estimate of $M_{b,\text{halo}}$.

Local Hot Bridge: One caveat arises from the possible existence of a ‘‘Local Hot Bridge,’’ a diffuse, X-ray, and SZ-bright plasma structure between the Milky Way and M31, first proposed by Bregman & Lloyd-Davies (2007). Qu et al. (2021) estimate the mass of the hot bridge to range over $6 \times 10^{10} M_{\odot}\text{--}7 \times 10^{11} M_{\odot}$ (see Figure 7 for a comparison with $M_{b,\text{halo}}$ measurements of M31 by other probes). This feature, inferred through angular geometry and modeled as a ≈ 400 kpc cylindrical filament, may contribute significantly to the total electron column density along sightlines toward M31. If real, it could add up to $\approx 100\text{--}400\text{ pc cm}^{-3}$ to the observed DM_{ext} , potentially contaminating or even dominating the DM attributed to M31’s halo. However, the existence and structure of this bridge are derived from model-dependent fits to X-ray and SZ residuals and thus remain hypothesis-driven. The inferred geometry is consistent with a large-scale intergalactic feature, but its contribution remains uncertain without direct absorption-line confirmation or off-axis FRB validation. Nonetheless, we emphasize that this possibility should be considered when interpreting DM measurements near M31,

and encourage future work to incorporate multi-wavelength tracers to better isolate individual plasma components.

Milky Way Halo Contribution: An additional source of uncertainty in our estimates of $\text{DM}_{\text{M31,halo}}$ arises from the contribution of the Milky Way’s halo. Ravi et al. (2025) estimate the $\text{DM}_{\text{MW,halo}}$ to be $\sim 38 \pm 19\text{ pc cm}^{-3}$, while Cook et al. (2023) report upper limits ranging from 52 to 119 pc cm^{-3} for high-latitude sightlines ($|b| \geq 30^{\circ}$). Given these significant systematic uncertainties, we elect not to subtract a specific value for the Milky Way halo contribution. Instead, we rely on the differential nature of our experiment: with over 800 FRBs in our final analysis set, we assume that the distribution of $\text{DM}_{\text{MW,halo}}$ is statistically similar for both M31 and control sightlines. This approach allows us to isolate the excess contribution from M31 via the weighted mean difference, while acknowledging residual uncertainties due to unmodeled variations in the Galactic halo. We note that Keating & Pen (2020) provide a detailed comparison of Milky Way halo models that could inform future analyses.

This is a limitation of our current results. In particular, if the Galactic halo were asymmetric in its DM contribution above and below the Galactic plane, this would confound the current analysis. With larger FRB samples, we may test for a radial dependence in the M31 signal from its center on the sky. An asymmetric Galactic halo would have to conspire to reproduce any such signature.

CHIME Sensitivity Variations: Because CHIME’s sensitivity varies across the sky, FRBs intersecting the M31 halo could be detected more efficiently than those in other regions, and therefore bias M31 FRBs towards higher DM. This introduces a potential systematic when comparing M31 FRBs and the control sample FRBs. We address this by incorporating a weighting scheme (Section 3.3) that accounts for differences in the DM_{ext} distributions, which are affected by sensitivity variation. Although CHIME is more sensitive toward declinations near M31, which could skew the M31-intersecting sample toward higher-DM FRBs, this weighting scheme mitigates that potential bias by reducing the influence of high-DM outliers on the inferred M31 signal.

5.4. Future Surveys

In our analysis, we have used a sample of arcminute-localized FRBs to estimate the δDM contributions of M31. We divided the halo into two radial bins and measured δDM with signal-to-noise ratios of 1.2 and 2.3. Our methodology supports further binning of the halo, enabling a more refined estimation of the δDM profile. However, increasing the number of bins with the current sample reduces the signal-to-noise ratio of δDM measured in each bin. To explore the potential of this approach in future surveys, we applied our methodology to simulated FRB samples of varying sizes. We found that for a sample of 20,000 FRBs (approximately 1,000 inter-

secting the M31 halo), with a sky distribution similar to the CHIME/FRB Catalog 2 sample (CHIME/FRB Collaboration et al. 2026), a δDM profile can be recovered with $> 90\%$ confidence using up to five bins.

Achieving the sample size of 20,000 FRBs that we considered in simulations will require sustained observations over the coming years. In the near term, CHIME/FRB is undergoing upgrades expected to increase its detection rate by a factor of ~ 3 , potentially yielding ~ 6 FRBs per day. At this rate, accumulating 20,000 FRBs would require approximately 5–6 years of continued operation, making CHIME a viable path to the sample sizes considered in our simulations.

Looking further ahead, next-generation wide-field surveys such as the Canadian Hydrogen Observatory and Radio-transient Detector (CHORD), the Bustling Universe Radio Survey Telescope in Taiwan (BURSTT), and the Deep Synoptic Array 2000 (DSA-2000) will dramatically increase global FRB detection rates. CHORD, expected to be fully operational by 2027, will provide broader frequency coverage and significantly higher sensitivity than CHIME, with forecasts indicating FRB detection rates up to a factor of 3–6 greater than CHIME/FRB’s current ~ 2 per day (CHORD in prep). DSA-2000, scheduled to begin operations in 2028, is expected to detect over 25,000 FRBs per year. However, as general-purpose survey instruments, neither CHORD nor DSA-2000 will be continuously observing the M31 region, so the fraction of their total FRB yield that probes M31 sightlines will depend on their sky coverage and survey strategy.

BURSTT, which began operations in mid-2025, features a vast field of view and is expected to double the detection rates. Importantly, its sensitivity to low-DM bursts makes it particularly valuable for probing nearby FRBs (Ling et al. 2023), where contributions from halos such as M31 are more prominent, thereby enhancing the measurable δDM signal.

Collectively, these instruments will rapidly expand the available FRB sample, though the rate at which M31-intersecting sightlines accumulate will depend not only on total detection rates but also on the sky coverage overlap with the M31 direction.

Beyond sample size, future surveys will provide improved FRB localizations and, in many cases, host galaxy identifications with spectroscopic redshifts. Instruments such as ASKAP and MeerTRAP already achieve sub-arcsecond localizations, enabling direct host associations and precise impact parameter measurements. For M31 specifically, localized FRBs with known redshifts would allow subtraction of the $\text{DM}_{\text{cosmic}}$ and DM_{host} contributions, isolating $\text{DM}_{\text{M31,halo}}$ on a sightline-by-sightline basis rather than statistically. The recent work by Anna-Thomas et al. (2025) demonstrates the power of this approach, achieving constraints on individual M31 sightlines that complement our statistical analysis.

Taken together, these facilities suggest that recovering the detailed δDM profile of M31 is well within reach: CHORD and DSA-2000 will deliver the large samples necessary, while BURSTT’s emphasis on nearby events offers a potent probe of the M31 halo. Combined with improved localizations from ASKAP and MeerTRAP, the next decade of FRB observations promises to transform our understanding of the CGM in M31 and other nearby galaxies.

6. CONCLUSION

This work has leveraged FRBs to statistically constrain the baryonic mass of M31’s CGM, a key but elusive reservoir that regulates galaxy evolution and baryon cycling. Traditional methods for probing the CGM face severe limitations, especially for nearby halos like M31. Our analysis demonstrates that FRBs offer a powerful, redshift-independent alternative.

Using a control sample of 684 FRBs and 171 M31 FRBs, we estimated the halo’s contribution to the dispersion measure (DM) by comparing to a control sample with similar Galactic DM. We constrained the M31 DM contribution, δDM , to $5.9\text{--}59.6\text{ pc cm}^{-3}$ and $25.7\text{--}64.6\text{ pc cm}^{-3}$ in radial bins of impact parameters spanning $\approx 0\text{--}151\text{ kpc}$ and $\approx 151\text{--}302\text{ kpc}$, respectively. We then used the parametric χ^2 framework with our generalized halo model to constrain the closure radius to $r_{\text{close}} = 9.2^{+19.2}_{-4.3} r_{\text{vir}} (1\sigma)$, corresponding to a total CGM mass of $M_{b,\text{halo}} = 18.6^{+7.9}_{-8.4} \times 10^{10} M_{\odot}$.

- Our measurements provide the first direct constraint on M31’s CGM mass using FRBs, and suggest the presence of a substantial ionized gas reservoir.
- While δDM estimates enable characterization of the baryon density profile, current uncertainties are still substantial in both radial bins, limiting our ability to resolve the profile in detail. We estimate that $\sim 20,000$ FRBs will be needed to constrain the radial structure of the CGM to a confidence limit $> 90\%$.
- Our analysis is based on a technique that requires only coarse FRB localizations and no host galaxy redshift information, making it scalable to future surveys.

Looking forward, as CHIME/FRB, ASKAP, MeerTRAP, and upcoming experiments like CHORD, BURSTT, and DSA-2000 expand the FRB sample size, we anticipate transformative improvements in CGM studies. Our method can be readily applied to other massive nearby halos, enabling a statistical inventory of circumgalactic baryons in the local universe.

These results represent a step toward establishing FRBs as precision tools for mapping diffuse baryons and unlocking the role of galaxy halos in the cosmic matter cycle.

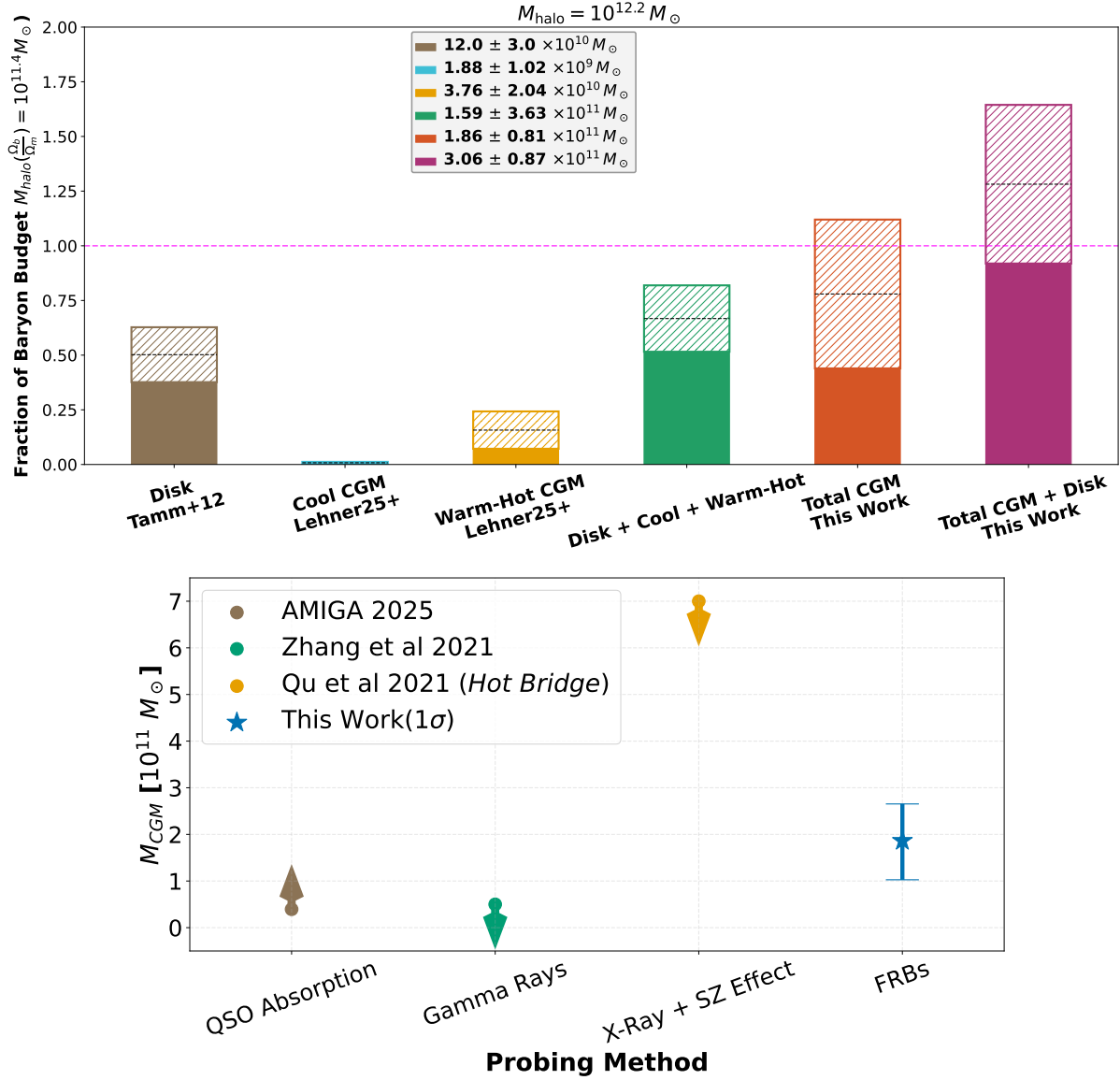


Figure 7. Top: Estimates of the baryonic content in different phases of the M31 system, shown as a fraction of the cosmic baryon budget $M_{b,\text{cosmic}} = M_{\text{halo}}(\Omega_b/\Omega_m) \approx 10^{11.4} M_\odot$. From left to right: stellar disk mass from Tamm et al. (2012); cool CGM mass from Lehner et al. (2025); warm-hot CGM mass from Lehner et al. (2025); combined disk + cool + warm-hot; total CGM mass from this work; and total CGM + disk from this work. Solid bars represent 1σ lower limits, while hatched regions indicate 1σ uncertainties. The horizontal dashed magenta line marks the cosmic baryon fraction. **Bottom:** Comparison of CGM mass estimates for M31 from different observational techniques. From left to right: QSO absorption-line measurements from AMIGA (Lehner et al. 2025); gamma-ray constraints from Zhang et al. (2021); X-ray + SZ effect upper limit on the “hot bridge” from Qu et al. (2021); and our FRB-based measurement (this work). Vertical bars indicate 1σ uncertainties; arrows indicate upper or lower limits. Our FRB measurement of $M_{b,\text{halo}} = 18.6^{+7.9}_{-8.4} \times 10^{10} M_\odot$ is consistent with the AMIGA lower bounds and the hot-bridge upper limit.

7. ACKNOWLEDGMENTS

Authors L.K., J.X.P., and S.S., as members of the Fast and Fortunate for FRB Follow-up team, acknowledge support from NSF grants AST-1911140 and AST-1910471. C. L. acknowledges support from the Miller Institute for Basic Research at UC Berkeley. A.B.P. acknowledges support by NASA through the NASA Hubble Fellowship grant HST-HF2-51584.001-A awarded by the Space Telescope Science Institute, which is operated by the Association of Universities for Research in Astronomy, Inc., under NASA contract NAS5-26555. A.B.P. also acknowledges prior support from a Banting Fellowship, a McGill Space Institute (MSI) Fellowship, and a Fonds de Recherche du Quebec – Nature et Technologies (FRQNT) Postdoctoral Fellowship. K.W.M. is supported by NSF Grant Nos. 2008031, 2510771 and holds the Adam J. Burgasser Chair in Astrophysics. E.F. is supported by the National Science Foundation (NSF) under grant number AST-2407399. The authors acknowledge helpful discussions with Mathew McQuinn, Isabel Medlock, Gwendolyn Eadie, and Raja Guhathakurta.

We acknowledge that CHIME and the k’ni?atn k’l_ stk’masqt Outrigger (KKO) are built on the traditional,

ancestral, and unceded territory of the Syilx Okanagan people. k’ni?atn k’l_ stk’masqt is situated on land leased from the Imperial Metals Corporation. We are grateful to the staff of the Dominion Radio Astrophysical Observatory, which the National Research Council of Canada operates. CHIME operations are funded by a grant from the NSERC Alliance Program and by support from McGill University, the University of British Columbia, and the University of Toronto. CHIME was funded by a grant from the Canada Foundation for Innovation (CFI) 2012 Leading Edge Fund (Project 31170) and by contributions from the provinces of British Columbia, Québec, and Ontario. The CHIME/FRB Project was funded by a grant from the CFI 2015 Innovation Fund (Project 33213) and by contributions from the provinces of British Columbia and Québec, and by the Dunlap Institute for Astronomy and Astrophysics at the University of Toronto. Additional support was provided by the Canadian Institute for Advanced Research (CIFAR), the Trottier Space Institute at McGill University, and the University of British Columbia. The CHIME/FRB baseband recording system is funded in part by a CFI John R. Evans Leaders Fund award to IHS.

Software: *astropy* (Astropy Collaboration et al. 2022), *pandas* (pandas development team 2020), and *numpy* (Harris et al. 2020)

APPENDIX

A. SENSITIVITY TO WEIGHTING PARAMETER α

In Section 3.3, we adopted a fiducial weighting parameter of $\alpha = 300 \text{ pc cm}^{-3}$ with $\beta = 1$ for our weighted estimator (Equation 13). Here we demonstrate that our main results are not sensitive to this choice by repeating our analysis for $\alpha = 150, 200, 400, 500,$ and 600 pc cm^{-3} .

The left panel of Figure 8 shows the non-parametric δDM estimates in the inner ($\approx 0\text{--}151 \text{ kpc}$) and outer ($\approx 151\text{--}302 \text{ kpc}$) radial bins as a function of α . The measured δDM values are consistent across all choices of α , with the fiducial $\alpha = 300$ (star markers) lying well within the range spanned by other values. The error bars increase for smaller α values, reflecting the reduced effective sample size when more aggressive downweighting is applied.

The right panel of Figure 8 shows the best-fit closure radius r_{close} as a function of α . The best-fit values range over $r_{\text{close}} \approx 9\text{--}13 r_{\text{vir}}$ across the explored range, with all values consistent within the 1σ uncertainties. The fiducial $\alpha = 300$ yields $r_{\text{close}} \approx 10 r_{\text{vir}}$, near the middle of this range. The 1σ confidence intervals overlap substantially for all α values, confirming that the choice of weighting parameter does not significantly affect our conclusions.

We conclude that our results are robust to the choice of α within the range $150\text{--}600 \text{ pc cm}^{-3}$. The fiducial value $\alpha = 300 \text{ pc cm}^{-3}$ lies within the optimal region identified in Figure 3 and provides a balance between variance reduction and signal retention.

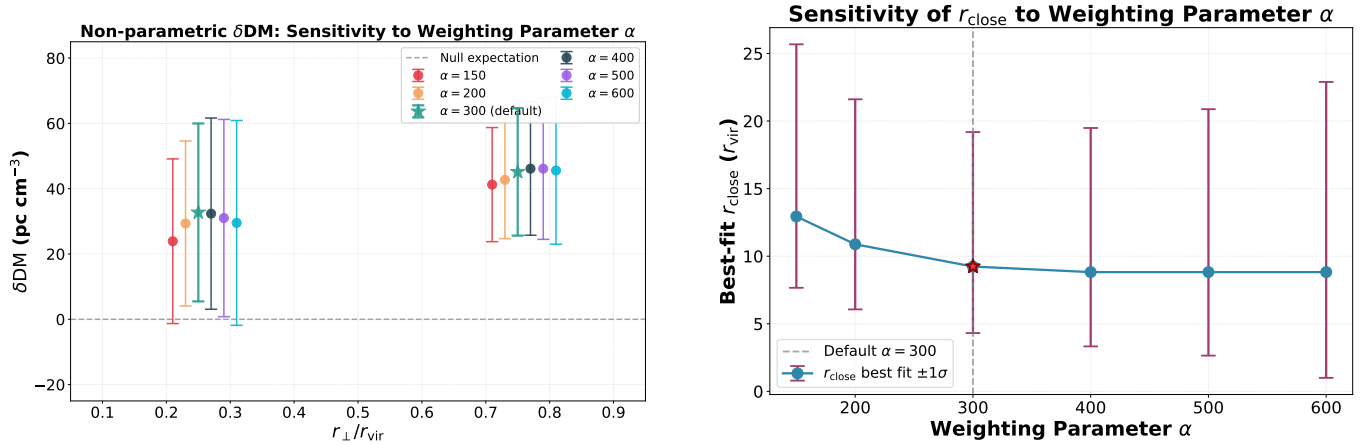


Figure 8. Left: Sensitivity of the non-parametric δDM estimates to the weighting parameter α . Points show the measured δDM in the inner (left, $0-0.5 r_{\text{vir}}$) and outer (right, $0.5-1 r_{\text{vir}}$) radial bins for $\alpha = 150, 200, 300, 400, 500$, and 600 pc cm^{-3} . The fiducial value $\alpha = 300$ is marked with a star. Error bars indicate 1σ uncertainties. The horizontal dashed line shows the null expectation ($\delta\text{DM} = 0$). Note that the horizontal offsets are for clarity, each error bar represents measurements for either the inner bin or the outer bin. **Right:** Sensitivity of the best-fit closure radius r_{close} to α . Blue points show the best-fit r_{close} values with 1σ error bars. The vertical dashed line marks $\alpha = 300$, with the best-fit shown as a red star. Both panels demonstrate that our conclusions are robust to the choice of α .

REFERENCES

- Anderson, M. E., & Bregman, J. N. 2011, *ApJ*, 737, 22, doi: [10.1088/0004-637X/737/1/22](https://doi.org/10.1088/0004-637X/737/1/22)
- Anna-Thomas, R., Law, C. J., Koch, E. W., et al. 2025, *ApJ*, 993, 221, doi: [10.3847/1538-4357/ae1014](https://doi.org/10.3847/1538-4357/ae1014)
- Astropy Collaboration, Price-Whelan, A. M., Lim, P. L., et al. 2022, *ApJ*, 935, 167, doi: [10.3847/1538-4357/ac7c74](https://doi.org/10.3847/1538-4357/ac7c74)
- Ayromlou, M., Nelson, D., & Pillepich, A. 2023, *MNRAS*, 524, 5391, doi: [10.1093/mnras/stad2046](https://doi.org/10.1093/mnras/stad2046)
- Behroozi, P., Wechsler, R. H., Hearin, A. P., & Conroy, C. 2019, *MNRAS*, 488, 3143, doi: [10.1093/mnras/stz1182](https://doi.org/10.1093/mnras/stz1182)
- Bordoloi, R., Tumlinson, J., Werk, J. K., et al. 2014, *ApJ*, 796, 136, doi: [10.1088/0004-637X/796/2/136](https://doi.org/10.1088/0004-637X/796/2/136)
- Bregman, J. N. 2007, *ARA&A*, 45, 221, doi: [10.1146/annurev.astro.45.051806.110619](https://doi.org/10.1146/annurev.astro.45.051806.110619)
- Bregman, J. N., Anderson, M. E., Miller, M. J., et al. 2018, *ApJ*, 862, 3, doi: [10.3847/1538-4357/aacafe](https://doi.org/10.3847/1538-4357/aacafe)
- Bregman, J. N., & Lloyd-Davies, E. J. 2007, *ApJ*, 669, 990, doi: [10.1086/521321](https://doi.org/10.1086/521321)
- Bryan, G. L., & Norman, M. L. 1998, *ApJ*, 495, 80, doi: [10.1086/305262](https://doi.org/10.1086/305262)
- Burchett, J. N., Tripp, T. M., Bordoloi, R., et al. 2016, *ApJ*, 832, 124, doi: [10.3847/0004-637X/832/2/124](https://doi.org/10.3847/0004-637X/832/2/124)
- Chatterjee, S., Law, C. J., Wharton, R. S., et al. 2017, *Nature*, 541, 58, doi: [10.1038/nature20797](https://doi.org/10.1038/nature20797)
- Chen, H.-W., & Zahedy, F. S. 2024, arXiv e-prints, arXiv:2412.10579, doi: [10.48550/arXiv.2412.10579](https://doi.org/10.48550/arXiv.2412.10579)
- Chen, H.-W., Zahedy, F. S., Boettcher, E., et al. 2020, *MNRAS*, 497, 498, doi: [10.1093/mnras/staa1773](https://doi.org/10.1093/mnras/staa1773)
- CHIME/FRB Collaboration, Amiri, M., Bandura, K., et al. 2018, *ApJ*, 863, 48, doi: [10.3847/1538-4357/aad188](https://doi.org/10.3847/1538-4357/aad188)
- CHIME/FRB Collaboration, Abbott, T., Andersen, B. C., et al. 2026, The Second CHIME/FRB Catalog of Fast Radio Bursts, arXiv, doi: [10.48550/arXiv.2601.09399](https://doi.org/10.48550/arXiv.2601.09399)
- CHIME/Pulsar Collaboration, Amiri, M., Bandura, K. M., et al. 2021, *ApJS*, 255, 5, doi: [10.3847/1538-4365/abfdcb](https://doi.org/10.3847/1538-4365/abfdcb)
- Chiu, I., Mohr, J. J., McDonald, M., et al. 2018, *MNRAS*, 478, 3072, doi: [10.1093/mnras/sty1284](https://doi.org/10.1093/mnras/sty1284)
- Connor, L., & Ravi, V. 2022, *Nature Astronomy*, 6, 1035, doi: [10.1038/s41550-022-01719-7](https://doi.org/10.1038/s41550-022-01719-7)
- Cook, A. M., Bhardwaj, M., Gaensler, B. M., et al. 2023, *ApJ*, 946, 58, doi: [10.3847/1538-4357/acbbd0](https://doi.org/10.3847/1538-4357/acbbd0)
- Cook, A. M., Li, D., Eadie, G. M., et al. 2024, arXiv e-prints, arXiv:2410.12146, doi: [10.48550/arXiv.2410.12146](https://doi.org/10.48550/arXiv.2410.12146)
- Cordes, J. M., & Lazio, T. J. W. 2002, arXiv e-prints, astro, <https://arxiv.org/abs/astro-ph/0207156>
- Courteau, S., Widrow, L. M., McDonald, M., et al. 2011, *ApJ*, 739, 20, doi: [10.1088/0004-637X/739/1/20](https://doi.org/10.1088/0004-637X/739/1/20)
- Dalcanton, J. J., Williams, B. F., Lang, D., et al. 2012, *ApJS*, 200, 18, doi: [10.1088/0067-0049/200/2/18](https://doi.org/10.1088/0067-0049/200/2/18)
- Dalcanton, J. J., Fouesneau, M., Hogg, D. W., et al. 2015, *ApJ*, 814, 3, doi: [10.1088/0004-637X/814/1/3](https://doi.org/10.1088/0004-637X/814/1/3)
- Faerman, Y., Sternberg, A., & McKee, C. F. 2020, *ApJ*, 893, 82, doi: [10.3847/1538-4357/ab7ffc](https://doi.org/10.3847/1538-4357/ab7ffc)
- Faerman, Y., & Werk, J. K. 2023, *ApJ*, 956, 92, doi: [10.3847/1538-4357/acf217](https://doi.org/10.3847/1538-4357/acf217)

- Faucher-Giguère, C.-A., & Oh, S. P. 2023, *Annual Review of Astronomy and Astrophysics*, 61, 131, doi: [10.1146/annurev-astro-052920-125203](https://doi.org/10.1146/annurev-astro-052920-125203)
- Fonseca, E., Andersen, B. C., Bhardwaj, M., et al. 2020, *ApJL*, 891, L6, doi: [10.3847/2041-8213/ab7208](https://doi.org/10.3847/2041-8213/ab7208)
- Harris, C. R., Millman, K. J., van der Walt, S. J., et al. 2020, *Nature*, 585, 357, doi: [10.1038/s41586-020-2649-2](https://doi.org/10.1038/s41586-020-2649-2)
- Howk, J. C., Wotta, C. B., Berg, M. A., et al. 2017, *ApJ*, 846, 141, doi: [10.3847/1538-4357/aa87b4](https://doi.org/10.3847/1538-4357/aa87b4)
- Huo, Z.-Y., Liu, X.-W., Xiang, M.-S., et al. 2013, *AJ*, 145, 159, doi: [10.1088/0004-6256/145/6/159](https://doi.org/10.1088/0004-6256/145/6/159)
- Josephy, A., Chawla, P., Curtin, A. P., et al. 2021, *ApJ*, 923, 2, doi: [10.3847/1538-4357/ac33ad](https://doi.org/10.3847/1538-4357/ac33ad)
- Keating, L. C., & Pen, U.-L. 2020, *MNRAS*, 496, L106, doi: [10.1093/mnras/slaa095](https://doi.org/10.1093/mnras/slaa095)
- Khrykin, I. S., Sorini, D., Lee, K.-G., & Davé, R. 2024a, *MNRAS*, 529, 537, doi: [10.1093/mnras/stae525](https://doi.org/10.1093/mnras/stae525)
- Khrykin, I. S., Ata, M., Lee, K.-G., et al. 2024b, arXiv e-prints, arXiv:2402.00505, doi: [10.48550/arXiv.2402.00505](https://doi.org/10.48550/arXiv.2402.00505)
- Komatsu, E., Smith, K. M., Dunkley, J., et al. 2011, *ApJS*, 192, 18, doi: [10.1088/0067-0049/192/2/18](https://doi.org/10.1088/0067-0049/192/2/18)
- Kravtsov, A. V., Vikhlinin, A. A., & Meshcheryakov, A. V. 2018, *Astronomy Letters*, 44, 8, doi: [10.1134/S1063773717120015](https://doi.org/10.1134/S1063773717120015)
- Kulkarni, S. R. 2020, arXiv e-prints, arXiv:2007.02886. <https://arxiv.org/abs/2007.02886>
- Lehner, N., Howk, J. C., & Wakker, B. P. 2015, *ApJ*, 804, 79, doi: [10.1088/0004-637X/804/2/79](https://doi.org/10.1088/0004-637X/804/2/79)
- Lehner, N., Berek, S. C., Howk, J. C., et al. 2020, *ApJ*, 900, 9, doi: [10.3847/1538-4357/aba49c](https://doi.org/10.3847/1538-4357/aba49c)
- Lehner, N., Howk, J. C., Collins, L., et al. 2025, arXiv e-prints, arXiv:2506.16573, doi: [10.48550/arXiv.2506.16573](https://doi.org/10.48550/arXiv.2506.16573)
- Lewis, A. R., Dolphin, A. E., Dalcanton, J. J., et al. 2015, *ApJ*, 805, 183, doi: [10.1088/0004-637X/805/2/183](https://doi.org/10.1088/0004-637X/805/2/183)
- Liang, C. J., & Chen, H.-W. 2014, *MNRAS*, 445, 2061, doi: [10.1093/mnras/stu1901](https://doi.org/10.1093/mnras/stu1901)
- Ling, D. F.-J., Hashimoto, T., Yamasaki, S., et al. 2023, *MNRAS*, 518, 1398, doi: [10.1093/mnras/stac3018](https://doi.org/10.1093/mnras/stac3018)
- Lorimer, D. R., Bailes, M., McLaughlin, M. A., Narkevic, D. J., & Crawford, F. 2007, *Science*, 318, 777, doi: [10.1126/science.1147532](https://doi.org/10.1126/science.1147532)
- Macquart, J. P., Prochaska, J. X., McQuinn, M., et al. 2020, *Nature*, 581, 391, doi: [10.1038/s41586-020-2300-2](https://doi.org/10.1038/s41586-020-2300-2)
- McGaugh, S. S., Schombert, J. M., de Blok, W. J. G., & Zagursky, M. J. 2010, *ApJL*, 708, L14, doi: [10.1088/2041-8205/708/1/L14](https://doi.org/10.1088/2041-8205/708/1/L14)
- McQuinn, M. 2014, *ApJL*, 780, L33, doi: [10.1088/2041-8205/780/2/L33](https://doi.org/10.1088/2041-8205/780/2/L33)
- . 2016, *ARA&A*, 54, 313, doi: [10.1146/annurev-astro-082214-122355](https://doi.org/10.1146/annurev-astro-082214-122355)
- Medlock, I., Nagai, D., Singh, P., et al. 2024, *ApJ*, 967, 32, doi: [10.3847/1538-4357/ad3070](https://doi.org/10.3847/1538-4357/ad3070)
- pandas development team, T. 2020, pandas-dev/pandas: Pandas, latest, Zenodo, doi: [10.5281/zenodo.3509134](https://doi.org/10.5281/zenodo.3509134)
- Patel, E., & Mandel, K. S. 2023, *ApJ*, 948, 104, doi: [10.3847/1538-4357/acc029](https://doi.org/10.3847/1538-4357/acc029)
- Péroux, C., & Howk, J. C. 2020, *ARA&A*, 58, 363, doi: [10.1146/annurev-astro-021820-120014](https://doi.org/10.1146/annurev-astro-021820-120014)
- Petroff, E., Bailes, M., Barr, E. D., et al. 2014, *MNRAS*, 447, 246, doi: [10.1093/mnras/stu2419](https://doi.org/10.1093/mnras/stu2419)
- Planck Collaboration, Aghanim, N., Akrami, Y., et al. 2020, *A&A*, 641, A6, doi: [10.1051/0004-6361/201833910](https://doi.org/10.1051/0004-6361/201833910)
- Pleunis, Z., Good, D. C., Kaspi, V. M., et al. 2021, *ApJ*, 923, 1, doi: [10.3847/1538-4357/ac33ac](https://doi.org/10.3847/1538-4357/ac33ac)
- Prochaska, J. X., Weiner, B., Chen, H. W., Mulchaey, J., & Cooksey, K. 2011, *ApJ*, 740, 91, doi: [10.1088/0004-637X/740/2/91](https://doi.org/10.1088/0004-637X/740/2/91)
- Prochaska, J. X., & Zheng, Y. 2019, *MNRAS*, 485, 648, doi: [10.1093/mnras/stz261](https://doi.org/10.1093/mnras/stz261)
- Prochaska, J. X., Werk, J. K., Worseck, G., et al. 2017, *ApJ*, 837, 169, doi: [10.3847/1538-4357/aa6007](https://doi.org/10.3847/1538-4357/aa6007)
- Putman, M. E., Peek, J. E. G., & Joung, M. R. 2012, *ARA&A*, 50, 491, doi: [10.1146/annurev-astro-081811-125612](https://doi.org/10.1146/annurev-astro-081811-125612)
- Qu, Z., Huang, R., Bregman, J. N., & Li, J.-T. 2021, *ApJ*, 907, 14, doi: [10.3847/1538-4357/abc9b9](https://doi.org/10.3847/1538-4357/abc9b9)
- Qu, Z., Chen, H.-W., Johnson, S. D., et al. 2024, *ApJ*, 968, 8, doi: [10.3847/1538-4357/ad410b](https://doi.org/10.3847/1538-4357/ad410b)
- Ravi, V., Catha, M., Chen, G., et al. 2025, *AJ*, 169, 330, doi: [10.3847/1538-3881/adc725](https://doi.org/10.3847/1538-3881/adc725)
- Renda, A., Kawata, D., Fenner, Y., & Gibson, B. K. 2005, *MNRAS*, 356, 1071, doi: [10.1111/j.1365-2966.2004.08530.x](https://doi.org/10.1111/j.1365-2966.2004.08530.x)
- Riess, A. G., Fliri, J., & Valls-Gabaud, D. 2012, *ApJ*, 745, 156, doi: [10.1088/0004-637X/745/2/156](https://doi.org/10.1088/0004-637X/745/2/156)
- Sorini, D., Davé, R., Cui, W., & Appleby, S. 2022, *MNRAS*, 516, 883, doi: [10.1093/mnras/stac2214](https://doi.org/10.1093/mnras/stac2214)
- Tamm, A., Tempel, E., Tenjes, P., Tihhonova, O., & Tuvikene, T. 2012, *A&A*, 546, A4, doi: [10.1051/0004-6361/201220065](https://doi.org/10.1051/0004-6361/201220065)
- Tchernyshyov, K., Werk, J. K., Wilde, M. C., et al. 2023, *ApJ*, 949, 41, doi: [10.3847/1538-4357/acc86a](https://doi.org/10.3847/1538-4357/acc86a)
- Tumlinson, J., Peebles, M. S., & Werk, J. K. 2017, *ARA&A*, 55, 389, doi: [10.1146/annurev-astro-091916-055240](https://doi.org/10.1146/annurev-astro-091916-055240)
- Tumlinson, J., Thom, C., Werk, J. K., et al. 2013, *ApJ*, 777, 59, doi: [10.1088/0004-637X/777/1/59](https://doi.org/10.1088/0004-637X/777/1/59)
- van der Marel, R. P., Fardal, M., Besla, G., et al. 2012, *ApJ*, 753, 8, doi: [10.1088/0004-637X/753/1/8](https://doi.org/10.1088/0004-637X/753/1/8)
- Wada, K., & Combes, F., eds. 2008, *Astrophysics and Space Science Proceedings*, Vol. 4, Mapping the Galaxy and Nearby Galaxies, doi: [10.1007/978-0-387-72768-4](https://doi.org/10.1007/978-0-387-72768-4)
- Werk, J. K., Prochaska, J. X., Thom, C., et al. 2013, *ApJS*, 204, 17, doi: [10.1088/0067-0049/204/2/17](https://doi.org/10.1088/0067-0049/204/2/17)
- Werk, J. K., Prochaska, J. X., Tumlinson, J., et al. 2014, *ApJ*, 792, 8, doi: [10.1088/0004-637X/792/1/8](https://doi.org/10.1088/0004-637X/792/1/8)

- Werk, J. K., Prochaska, J. X., Cantalupo, S., et al. 2016, *ApJ*, 833, 54, doi: [10.3847/1538-4357/833/1/54](https://doi.org/10.3847/1538-4357/833/1/54)
- Wilde, M. C., Werk, J. K., Burchett, J. N., et al. 2021, *ApJ*, 912, 9, doi: [10.3847/1538-4357/abea14](https://doi.org/10.3847/1538-4357/abea14)
- Williams, B. F., Dalcanton, J. J., Bell, E. F., et al. 2012, *ApJ*, 759, 46, doi: [10.1088/0004-637X/759/1/46](https://doi.org/10.1088/0004-637X/759/1/46)
- Williams, B. F., Dolphin, A. E., Dalcanton, J. J., et al. 2017, *ApJ*, 846, 145, doi: [10.3847/1538-4357/aa862a](https://doi.org/10.3847/1538-4357/aa862a)
- Wu, X., & McQuinn, M. 2023, *ApJ*, 945, 87, doi: [10.3847/1538-4357/acbc7d](https://doi.org/10.3847/1538-4357/acbc7d)
- Yao, J. M., Manchester, R. N., & Wang, N. 2017, *ApJ*, 835, 29, doi: [10.3847/1538-4357/835/1/29](https://doi.org/10.3847/1538-4357/835/1/29)
- Zhang, Y., Liu, R.-Y., Li, H., et al. 2021, *ApJ*, 911, 58, doi: [10.3847/1538-4357/abe9b6](https://doi.org/10.3847/1538-4357/abe9b6)
- Zhang, Y., Comparat, J., Ponti, G., et al. 2024a, *A&A*, 690, A268, doi: [10.1051/0004-6361/202449413](https://doi.org/10.1051/0004-6361/202449413)
- . 2024b, *A&A*, 690, A267, doi: [10.1051/0004-6361/202449412](https://doi.org/10.1051/0004-6361/202449412)
- Zheng, Y., Faerman, Y., Oppenheimer, B. D., et al. 2024, *ApJ*, 960, 55, doi: [10.3847/1538-4357/acfe6b](https://doi.org/10.3847/1538-4357/acfe6b)

All Authors and Affiliations

LORDRICK A. KAHINGA ^{1,2} J. XAVIER PROCHASKA ^{1,3,4} SUNIL SIMHA ^{5,6,*} CALVIN LEUNG ^{7,†} RADU V. CRAIU ⁸
GWENDOLYN. EADIE ^{9,8} EMMANUEL FONSECA ^{10,11} B. M. GAENSLER ^{1,9,12} VICKY KASPI ^{13,14} AFROKK KHAN ^{13,14}
BIKASH KHAREL ^{8,10,11} ADAM E. LANMAN ^{15,16} ROBERT A. MAIN ^{13,14} LLUIS MAS-RIBAS ¹ KIYOSHI W. MASUI ^{15,16}
PAUL SCHOLZ ¹⁷ SWARALI SHIVRAJ PATIL ^{10,11} AARON B. PEARLMAN ^{15,16,13,14,‡} K. SHIN ¹⁸ SETH R. SIEGEL ^{19,13,14}
KENDRICK SMITH ¹⁹ AND MICHELE WOODLAND ¹

¹Department of Astronomy and Astrophysics, University of California, Santa Cruz, 1156 High Street, Santa Cruz, CA 95064, USA

²Department of Physics, College of Natural and Mathematical Sciences, University of Dodoma, Dodoma, P.O. Box 259, Tanzania

³Kavli Institute for the Physics and Mathematics of the Universe (Kavli IPMU), 5-1-5 Kashiwanoha, Kashiwa, 277-8583, Japan

⁴Division of Science, National Astronomical Observatory of Japan, 2-21-1 Osawa, Mitaka, Tokyo 181-8588, Japan

⁵Center for Interdisciplinary Exploration and Research in Astronomy, Northwestern University, 1800 Sherman Avenue, Evanston, IL 60201, USA

⁶Department of Astronomy and Astrophysics, University of Chicago, William Eckhart Research Center, 5640 South Ellis Avenue, Chicago, IL 60637, USA

⁷Department of Astronomy, University of California, Berkeley, CA 94720, United States

⁸Department of Statistical Sciences, University of Toronto, 700 University Ave., Toronto, ON M5G 1Z5, Canada

⁹David A. Dunlap Department of Astronomy and Astrophysics, 50 St. George Street, University of Toronto, ON M5S 3H4, Canada

¹⁰Department of Physics and Astronomy, West Virginia University, PO Box 6315, Morgantown, WV 26506, USA

¹¹Center for Gravitational Waves and Cosmology, West Virginia University, Chestnut Ridge Research Building, Morgantown, WV 26505, USA

¹²Dunlap Institute for Astronomy and Astrophysics, 50 St. George Street, University of Toronto, ON M5S 3H4, Canada

¹³Department of Physics, McGill University, 3600 rue University, Montréal, QC H3A 2T8, Canada

¹⁴Trottier Space Institute, McGill University, 3550 rue University, Montréal, QC H3A 2A7, Canada

¹⁵MIT Kavli Institute for Astrophysics and Space Research, Massachusetts Institute of Technology, 77 Massachusetts Ave, Cambridge, MA 02139, USA

¹⁶Department of Physics, Massachusetts Institute of Technology, 77 Massachusetts Ave, Cambridge, MA 02139, USA

¹⁷Department of Physics and Astronomy, York University, 4700 Keele Street, Toronto, ON M3J 1P3, Canada

¹⁸Cahill Center for Astronomy and Astrophysics, MC 249-17 California Institute of Technology, Pasadena CA 91125, USA

¹⁹Perimeter Institute of Theoretical Physics, 31 Caroline Street North, Waterloo, ON N2L 2Y5, Canada